DEPARTAMENT OF
CHEMISTRY

NOVA SCHOOL OF
SCIENCE & TECHNOLOGY

NUNO MARIA REIS FERREIRA
BSc in Biochemistry

Plasmonic Nanostars for Sensitive SERS-based Glial Fibrillary Acidic Protein Immunodetection

MASTER IN BIOTECHNOLOGY
NOVA University Lisbon
<month>, <year>

NOVA SCHOOL OF SCIENCE & TECHNOLOGY

DEPARTAMENT OF CHEMISTRY

NUNO MARIA REIS FERREIRA

BSc in Biochemistry

Adviser: José Ricardo Ramos Franco Tavares
Associate Professor, NOVA University Lisbon

Co-advisers: Hugo Águas
Associate Professor, NOVA University Lisbon

Examination Committee:

Chair: Name of the committee chairperson,
Full Professor, FCT-NOVA

Rapporteurs: Name of a rapporteur,
Associate Professor, Another University
Name of another rapporteur,
Assistant Professor, Another University

Adviser: Name of the adviser present in defense,
Associate Professor, University

Members: Yet another member of the committee,
Full Professor, Another University
Yet another member of the committee,
Assistant Professor, Another University

MASTER IN BIOTECHNOLOGY

NOVA University Lisbon
<month>, <year>

Plasmonic Nanostars for Sensitive SERS-based Glial Fibrillary Acidic Protein Immunodetection

Acknowledgments

First of all, I would like to thank Professors Ricardo Franco and Hugo Águas for giving me the opportunity to work in this lab during the past year.

I would like to thank my adviser Professor Ricardo Franco for welcoming me in his lab, for all the insightful discussions and guidance throughout this year.

To my co-adviser Professor Hugo Águas for their helpful comments and suggestions.

A big thanks to everyone in Bionanotechnology lab, for hearing my rants and daily troubles! To Oana, for giving an engineer's point-of-view on an all-bio lab and for all the wordles and heardles solved. To Simão, for the helpful suggestions and discussions. A big thank you to Cristina, my lab partner and lunch buddy, for bringing so many snacks and sweets that balanced out the stress, for the daily conversations and good mood even when things went wrong! To Hugo, for letting me teach what little I know of the subject and for being a helping hand during his stay.

Finally, last but not least, to Susana for always being there to hear me rant about what went wrong that day, for letting me brainstorm off of her even if she did not understand anything that I was saying and for being an emotional support during this phase of my life. A huge thank you because I would have not been able to do this without you!

ABSTRACT

Worldwide, TBI is estimated to affect 64-74 million individuals, or around 759 per every 100.000 people, mostly in developing countries, and is often called the “silent epidemic”, leading to neurodegenerative diseases such as Alzheimer’s. Quick TBI diagnosis is of extreme importance to assure the best chances for a full recovery, avoiding dangerous complications. Point-of-care testing platforms (POTC) are needed in such cases, where most of these accidents occur and easy access to the necessary diagnosis equipment is not common. Therefore, in this work, a method for the ultrasensitive detection of Glial Fibrillary Acidic Protein (GFAP) in blood, is explored, by combining gold nanostars (AuNS) functionalized with 4-mercaptobenzoic acid with Surface Enhanced Raman Spectroscopy (SERS), to enable quantification of the GFAP on a blood sample. This thesis also explores the formation of gold nanosphere (AuNP) conjugates for the colorimetric and qualitative analysis of GFAP. Due to the anti-GFAP antibody inducing aggregation, anti-HRP was used to form both AuNP and AuNS conjugates for the detection of HRP, and for further testing. This serves as a proof-of-concept and for optimisation with a model antibody, optimising the loading concentration of both antibody and blocking protein (BSA) by agarose gel electrophoresis (AGE), UV-Vis, Dynamic Light Scattering and enzymatic activity assays. Sensitivity tests were made using anti-HRP and HRP, with a visual cutoff value of 180 ng for the qualitative part. The cutoff value for the quantitative part of the assay, using SERS analysis, was assessed to be around the same values, between 180 and 60 ng, by calculating the peak integral of the 1589 cm^{-1} 4-MBA peak. In the end, promising results were obtained, needing the shift from the model antibody to the anti-GFAP antibody for accurate detection of TBI in blood. Obtaining a quick, POCT diagnosis tool such as an LFA would help alleviate the burden of hospitals in developed countries, avoid missed diagnosis and provide with an easy to use, cheap, easily storable and easily shipped tool for developing countries where this issue is most prevalent in the world, contributing to the decrease of this “silent epidemic”.

Keywords: Traumatic brain Injury, Glial Fibrillary Acidic Protein, Lateral flow assay, Surface enhanced Raman scattering, Gold nanostars, Gold nanoparticles

Resumo

Em todo o mundo, estima-se que o traumatismo cranioencefálico (TCE) afete entre 64 a 74 milhões de indivíduos, ou cerca de 759 por cada 100.000 pessoas, maioritariamente em países em desenvolvimento, sendo frequentemente denominado a "epidemia silenciosa", uma vez que pode levar a doenças neurodegenerativas como a doença de Alzheimer. Um diagnóstico rápido de TCE é de extrema importância para assegurar as melhores hipóteses de uma recuperação completa, evitando complicações perigosas. Plataformas de testes no ponto de cuidado (POCT) são necessárias nesses casos, onde a maioria destes acidentes ocorre e o acesso fácil ao equipamento de diagnóstico necessário não é comum. Assim, neste trabalho, é explorado um método para a deteção ultra-sensível da Proteína Glial Fibrilar Ácida (GFAP) no sangue, combinando nanoestrelas de ouro (AuNS) funcionalizadas com ácido 4-mercaptobenzoico com Espectroscopia Raman Intensificada por Superfície (SERS), para permitir a quantificação de GFAP numa amostra de sangue. Esta tese também explora a formação de conjugados de nanospheres de ouro (AuNP) para a análise colorimétrica e qualitativa de GFAP. Devido à indução de agregação pelo anticorpo anti-GFAP, foi utilizado o anticorpo anti-HRP para formar conjugados de AuNP e AuNS para a deteção de HRP. Isto serve como prova de conceito e para a optimização com um anticorpo modelo, optimizando a concentração de carga de ambos, o anticorpo e a proteína de bloqueio (BSA), através de eletroforese em gel de agarose (AGE), UV-Vis, Dispersão de Luz Dinâmica e ensaios de atividade enzimática. Foram realizados testes de sensibilidade usando anti-HRP e HRP, com um valor de corte visual entre 180 ng e 60 ng para a parte qualitativa. O valor de corte para a parte quantitativa do ensaio, usando a análise SERS, foi estabelecido dentro dos mesmos valores, entre 180 ng e 60 ng, através do cálculo do integral do pico de 1589 cm-1 do pico do 4-MBA. No final, foram obtidos resultados promissores, sendo necessário passar do anticorpo modelo para o anticorpo anti-GFAP para a deteção precisa de TCE no sangue. Obter uma ferramenta de diagnóstico rápido POCT, como um LFA, ajudaria a aliviar a sobrecarga nos hospitais dos países desenvolvidos, evitar diagnósticos falhados e fornecer uma ferramenta fácil de usar, barata, facilmente armazenável e facilmente transportável para os países em desenvolvimento, onde este problema é mais prevalente no mundo, contribuindo para a diminuição desta "epidemia silenciosa".

Palavras chave: Traumatismo cranioencefálico, Proteína Glial Fibrilar Ácida, Imunoensaio de fluxo lateral, Espalhamento Raman Intensificado por Superfície, Nanoestrelas de ouro, Nanopartículas de ouro

Table of Contents

List of figures

List of tables

List of abbreviations

BCA - Bicinchoninic Acid

TBI – Traumatic Brain Injury

HSA - Human Serum Albumin

LFA - Lateral Flow Assay

AuNP - Gold Nanoparticles

AuNS - Gold Nanostars

AGE - Agarose Gel Electrophoresis

BSA - Bovine Serum Albumin

EDC - 1-Ethyl-3-(3-dimethylaminopropyl)carbodiimide

SNHS - N-Hydroxysuccinimide

SERS - Surface-Enhanced Raman Scattering

GFAP - Glial Fibrillary Acidic Protein

HRP - Horseradish Peroxidase

MUA - Mercaptoundecanoic Acid

PBS - Phosphate Buffered Saline

PDI - Polydispersity Index

SPR - Surface Plasmon Resonance

UV-Vis - Ultraviolet–Visible Spectroscopy

DLS - Dynamic Light Scattering

LSPR - Localized Surface Plasmon Resonance

CT - Computed Tomography

MRI - Magnetic Resonance Imaging

LoD - Limit of Detection

LoQ – Limit of Quantification

ABTS - 2,2'-Azino-bis(3-ethylbenzothiazoline-6-sulfonic acid)

KD – Dissociation constant

KPB - Potassium Phosphate Buffer

4-MBA - 4-Mercaptobenzoic Acid

11-MUA – 11-Mercaptoundecanoic acid

UCH-L1 - Ubiquitin C-terminal Hydrolase L1

NF-L - Neurofilament Light

Aβ - Amyloid Beta

BBB - Blood-Brain Barrier

ENS - Enteric Nervous System

CNS - Central Nervous System

POCT - Point-of-Care Testing

S100B - S100 Calcium-Binding Protein B

T-tau - Total Tau

WHO - World Health Organization

ELISA - Enzyme-Linked Immunosorbent Assay

Symbols

A – Absorbance

Δμ - Variations relative to the maximum mobility band

E - Strength of the driving field

E - Extinction molar coefficient

$\boldsymbol{KD}$ - Dissociation constant

V - Velocity

1. Introduction

1.1. Traumatic Brain Injury

1.1.1. Incidence

Traumatic brain injury (TBI) is one of the most important cerebral pathologies encountered nowadays, contributing the most to death and disability than any other traumatic insult[1]. This disease, often called the "silent epidemic", is caused by receiving a bump, blow or jolt to the head or a penetrating head injury that results in the disruption of normal brain function[2]. Worldwide, TBI is estimated to affect 64-74 million individuals, or around 759 per every 100.000 people[3]. From those cases, the majority of TBI cases caused by road accidents is attributed to Africa and Southeast Asia. Proportionately, low to medium income countries suffer 3 times as many cases of TBI as high income countries, however the biggest incidence of TBI belongs to Europe and the United States of America with 1012 and 1299 cases per 100.000 people respectively, in 2017[1], as can be seen in figure 1. In 2020 and 2021, there were approximately 214.110 TBI related hospitalizations and 69,473 TBI-related deaths in the USA, not counting those that go unnoticed or are treated without hospitalization (in emergency care or in ambulances, for example), according to the Centre for Disease Control (CDC)[4].

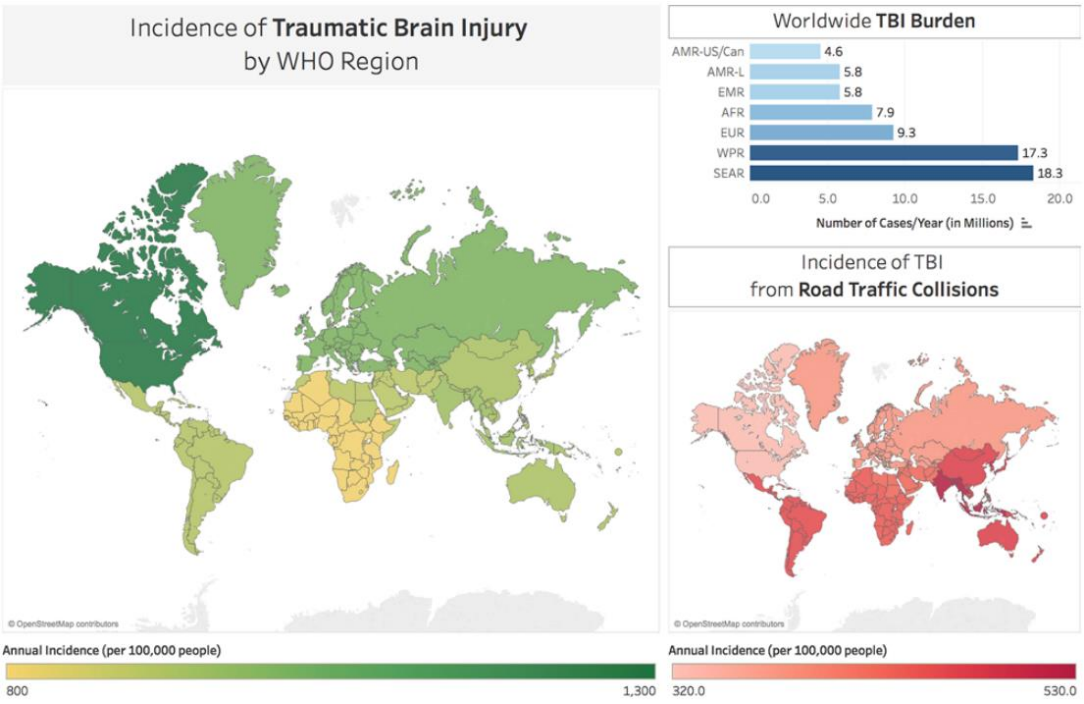

Figure 1 - Map showing the incidence of TBI per 100 000 people, per World Health Organization region, on the left. Upper right, estimation of volume of TBI cases annually across WHO regions. On the lower right, annual incidence of TBI, per 100 000 people, attributed to traffic accidents per WHO region. Reprinted from M. C. Dewan et al., 'Estimating the global incidence of traumatic brain injury', J Neurosurg, vol. 130, no. 4, pp. 1080–1097, Apr. 2018.

Even with some lack of information and study quality about TBI in low to medium income countries [1], it is possible to assess that this injury is a very much present around the world, leaving the injured with major side effects like age-related neurodegenerative disorders such as Alzheimer's disease and chronic traumatic encephalopathy [5], which leads to long-term memory and cognition issues[6].

1.1.2. TBI types and symptoms

TBI can be separated into 2 broad categories of injury: penetrating and non-penetrating, with the difference being whether or not the source of the injury penetrated the skull and entered the brain tissue, damaging only part of the brain[7].

To further differentiate between TBI cases, it can be classified as mild, moderate, or severe based on the effect of the injury on the brain:

Mild traumatic brain injury:

- Physical symptoms: traumatic brain injury which is characterized by physical symptoms such as headache, nausea or vomiting, fatigue or drowsiness and dizziness or loss of balance.

- Sensory symptoms: blurred vision, ringing in the ears, bad taste in the mouth, changes in the ability to smell and sensitivity to light or sound.

- Cognitive, behavioural or mental symptoms: Loss of consciousness from a few seconds to a few minutes, confusion or disorientation, memory or concentration problems, mood changes and swings, depression and anxiety, difficulty sleeping or oversleeping.

Moderate to severe brain injuries:

- Physical symptoms: Loss of consciousness from several minutes to hours, persistent headaches, repeated vomiting and nausea, convulsions or seizures, dilation of eye pupils, clear fluids draining from the nose or ears, inability to wake up from sleep, weakness or numbness in fingers and toes and loss of coordination.
- Cognitive or mental symptoms: profound confusion, agitation and unusual behaviour, slurred speech and coma or other consciousness disorders.

In addition to all this, many complications can quickly arise after a traumatic brain injury which can lead to problems such as strokes, permanent brain damage and even death[8].

1.1.2.1. Diagnosis methods

When a concussion happens, it is necessary to get diagnosed as soon as possible. As the treatment is based on the severity of the injury, it is necessary to know if it is mild or moderate to severe as mild injuries are usually treated with over-the-counter headache painkillers and close monitoring for worsening symptoms, while moderate to severe injuries need immediate emergency care as such traumas are followed by secondary effects such as seizures, brain swelling, blood clots or brain bleeding [9].

The diagnosis is usually made by imaging tests such as computerized tomography (CT) scan, where a series of X-rays from different angles are used to create a detailed view of the brain[10], and magnetic resonance imaging (MRI) that uses radio waves and magnetic fields to produce detailed images of the brain [11]. These have secondary effects such as the use of radiation and/or contrast and low sensitivity to diffuse brain damage in case of CT scans, or heating, inability to have magnetic prosthetics and other limitations associated with MRI[12]. Furthermore, correct diagnosis of TBI severity is indispensable as patients with seemingly similar TBI incurring injuries can have wildly different outcomes [13].

To avoid the lack of sensitivity of current diagnostic methods, the requirement of specialist handling or the involvement of complicated and costly procedures, new ways of obtaining a point-of-care have been investigated, such as the detection of biomarkers in biofluids[14].

1.1.3.Biomarkers for TBI

Biomarkers are, most simply, biological markers, indicators of the body's response to medicine, pathogens or any biological process happening inside the body that can be measured objectively and accurately[15].

A number of biomarkers for TBI have been discovered throughout the years, with most of the data being obtained by measurements in the cerebral spinal fluid (CSF), blood and some in saliva[13]. Currently, the known biomarkers related to brain trauma are as follows:

- S100B, a calcium-binding protein, is widely expressed in the brain, in the most part by astrocytes but also by other brain cells in much smaller quantities. When brain damage occurs, this protein is released extracellularly, becoming available in the serum. Currently, S100B is the most used protein for diagnostics, however its extra-astrocytic and extracerebral expression limit is use in diagnostics [16].

- Ubiquitin C-terminal hydrolase-L1 (UCH-L1) is detectable within 1 hour of TBI, peaking at 8 hours after injury, with a half-life of 7-9hours, being expressed by neurons but also by cells outside of the CNS (Central nervous system). It was capable of discriminating CT-Negative from CT-Positive patients, however there are some reports that UCH-L1 was not capable of distinguish healthy controls from patients with mTBI[17].

- Tau, a microtubule-associated protein located in the axons of CNS neuros. Plasma total Tau (T-tau) values in plasma have been correlated with the outcome of repeated mTBI or concussion and it has also been a good predictor of severe TBI outcome. However, T-tau has been unable to differentiate CT-Positive from CT-Negative mild TBI cases[17].

- Neurofilament light (NF-L) is expressed in the long myelinated white matter axons of the brain or peripheral axons. Studies made with this biomarker have shown that it has good correlation between its early plasma levels and the outcome of patients with mild TBI, showing that it can be a good biomarker for tracking neurodegenerative progress. However, this protein takes between 10 days and 6 weeks to achieve its peak concentration, making it difficult to use for point-of-care[17].

- Aβ reflect amyloidogenic amyloid precursor protein metabolism and may be potential biomarkers of axonal damage in TBI, however, plasma values have not shown good capability of identifying CT-positive mild TBI cases or predicting the outcome of the mild TBI[18].

- GFAP, which will be the focus of the next chapter.

1.1.4. Glial Fibrillary Acidic Protein as a TBI biomarker

Astrocytes represent around 30-40% of the cells in the central nervous system (CNS), form an important part of the blood brain barrier (BBB) and create interactions with many other cells in the nervous system, including neurons[19]. GFAP is an intermediate filament-III protein found solely in astrocytes in the central nervous system (CNS), non-myelinating Schwann cells in the peripheral nervous system and enteric glial cells in the enteric nervous system (ENS)[20]. When a brain injury which causes astrocyte injury or death occurs, GFAP, which is not usually present in high concentrations in blood, is more heavily secreted, which makes it ideal for use as a TBI identifying biomarker[12], as exemplified in figure 2.

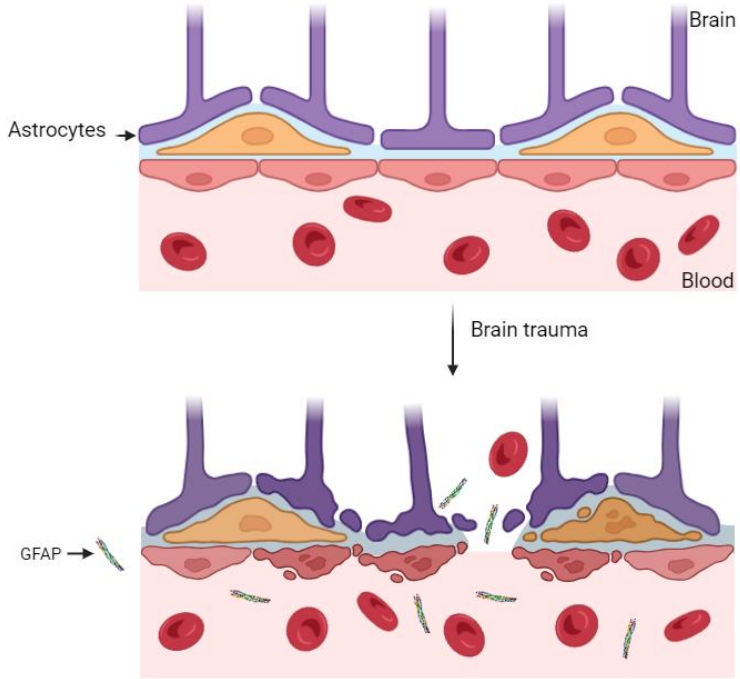

Figure 2- Impact of brain trauma on the blood brain barrier and example of the release of GFAP to the blood, caused by astrocyte GFAP production and the disruption of the blood brain barrier. Figure made in BioRender.

GFAP demonstrates some appealing characteristics for use as a biomarker, such as a high increase in blood concentration in the range of 0-12h which is ideal for a point-of-care diagnosis, and higher half-life time than the Tau and UCH-L1 proteins, as shown in figure 3. To further cement its promising aspect as a TBI diagnostics tool, in a study of 2000 non-penetrating TBI, 66% of patients had a concentration of GFAP in blood of over 22 pg/mL, with a test sensitivity of 0.976 and a negative predictive value of 0.996 [21]. In another study, GFAP had a better predictive capability of pathological head CT results when compared to other biomarkers such as UCH-L1 and the current standard biomarker for TBI diagnosis, SB100, with a sensitivity of around 0.9 and specificity of 0.64 in the 0-34h mark following injury[22]. This protein was also capable of predicting CT abnormalities in older adults (>50 years old) [23] where the basal GFAP production is higher when compared to younger patients. [24].

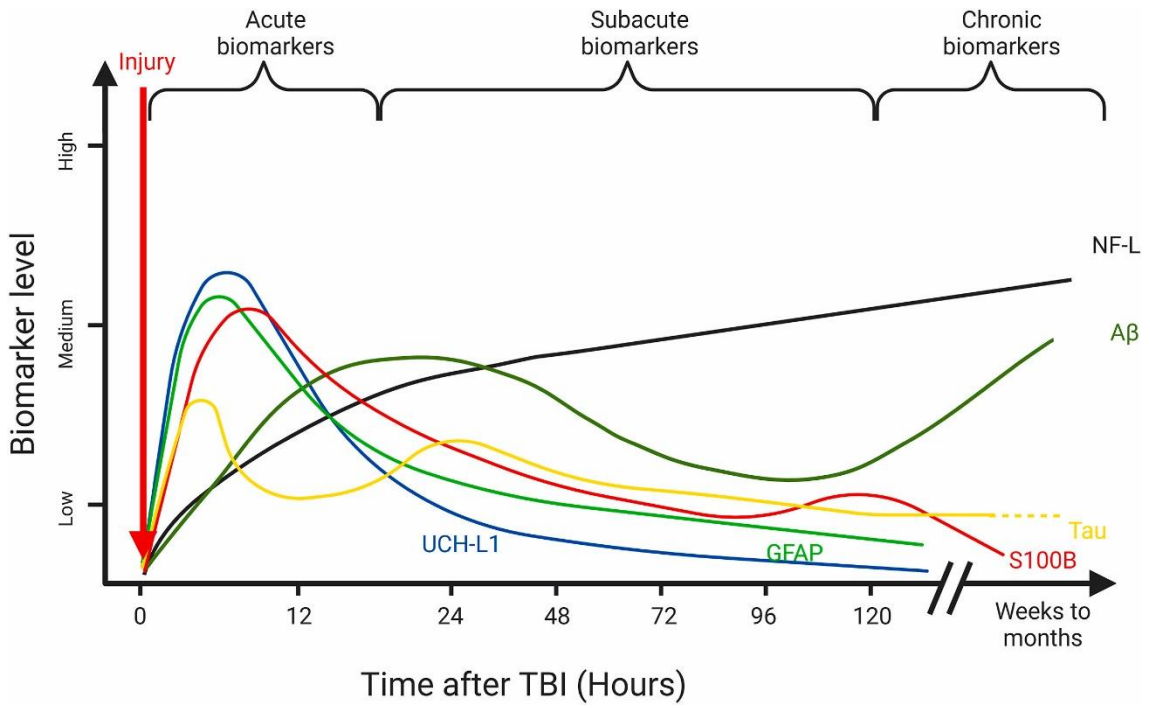

Figure 3 – Approximate levels of TBI biomarkers over time and acuteness designation. Image taken from Hossain, Niklas Marklund, Endre Czeiter, P. Hutchinson, and Andras Buki, "Blood biomarkers for traumatic brain injury: A narrative review of current evidence," Brain and Spine, vol. 4, pp. 102735–102735, Jan. 2024, doi: https://doi.org/10.1016/j.bas.2023.102735.

As we can see from the time frame where the protein in present in the blood, and also from the fact that non-treated brain trauma can cause long-term consequences such as brain atrophy and increased vulnerability to neurodegenerative disorders[5], a fast diagnosis tool is needed.

1.2. Lateral Flow Immunoassay (LFIA)

Lateral flow assays are a technology based on paper as a platform for the detection and/or quantification of the analyte in complex mixtures, such as blood, urine or mucus, for example [25].

This technology has been steadily increasing in value over the years, having had a very big jump in exposure and investment during the Covid-19 pandemic, and being projected to still increase during the next few years [26]. This is due to their ease of use, the fact that they do not need to be refrigerated, are low-cost in fabrication, are of easy transportation, do not need laboratory trained people to

perform them and are usually easy to perform and to analyse, taking only a few minutes to display the result [25].

These tests are usually composed of 5 to 6 elements, also exemplified in figure 4, and these are:

- The fiberglass pad, which acts as a filter to remove erythrocytes and large blood components from the sample when working with blood samples, to avoid blocking the flow on the membrane, usually placed on top of the sample pad when necessary.
- The sample pad, which is where the sample is going to be first absorbed into.
- The conjugate pad or conjugate release pad, where the sample with the biomarker will mix with the pre-adsorbed nanoparticle and antibody conjugates, and then flow onto the nitrocellulose membrane.
- The nitrocellulose membrane, where the test and control lines are prepared and where the sample will flow through.
- The absorption pad, which will help with the capillarity of the system and the flow rate of the sample.

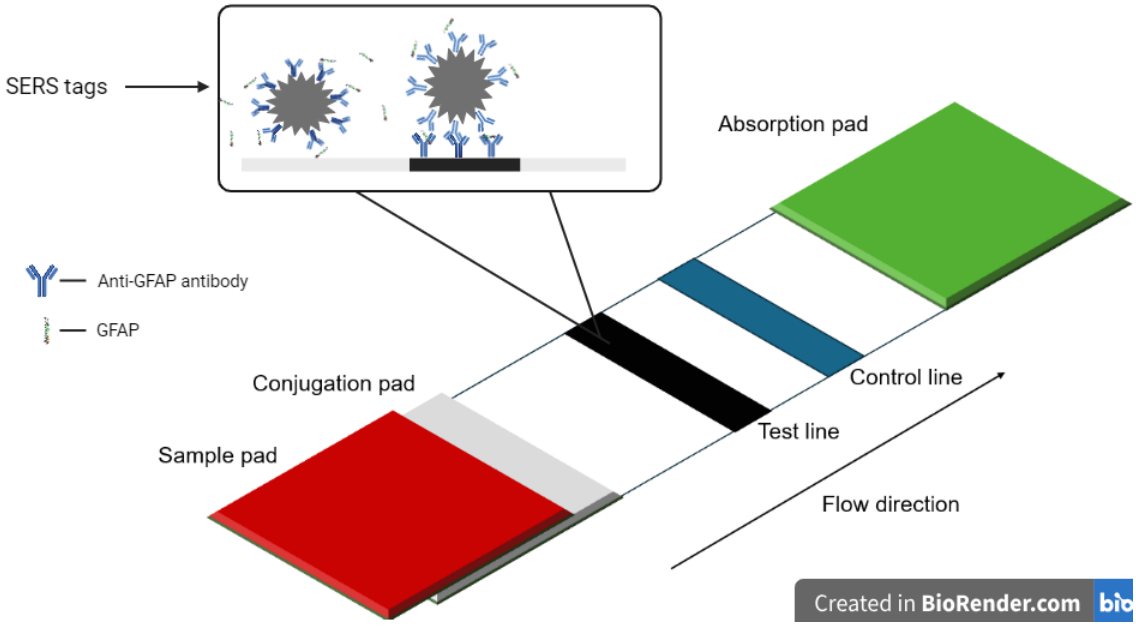

Figure 4 - Configuration of a sandwich type lateral flow assay for GFAP detection using gold nanostars covered with anti-GFAP antibodies, 4-mercaptobenzoic acid (MBA) and mixed with a GFAP positive sample. The test line is composed of anti-GFAP IgG for specific detection of GFAP, and the control line composed of anti-IgG antibodies for the detection of the AuNSs not bound to the test line. Figure made in BioRender.

Lateral flow immunoassays can be separated into 2 different types of assays:

- **Competitive**, used for small analytes which donot have more than one antigen binding site. An analogue of the target molecule is immobilized on the nitrocellulose membrane test line, and, in the absence of the target molecule, the signalling tags will bind to the test line and increase its signal. More target molecule in the sample, will produce a less intense signal [27].

- **Sandwich,** used for larger analytes with more than one antigen binding site, where antibodies specific for the antigen are immobilized on the test line. The sample is mixed with the signalling tags (in the work developed here, anti-GFAP antibody covered AuNSs) and, in case of a positive signal, there will be the appearance of a coloured test line. If negative, only the control line, composed of anti-Immunoglobulin G (IgG) antibodies and antibody:AuNSs conjugates, will appear. The end result of this type of assay is exemplified in figure 4[27].

The development of these tests is of high importance since, for the reasons mentioned before, these make strong candidates for point-of-care (POC) use, as their implementation for detecting specific antigens makes for a quick diagnosis tool in an environment where time efficiency is of upmost importance.

1.2.1.IgG Antibodies

Antibodies are mainly composed of 2 parts, the constant region, which as the name suggests does not vary inside the IgG antibody isotype, and the variable region, which changes from antibody to antibody inside its isotype to be specific to its specific target antigen, as exemplified in figure 5. Due to this, an anti-horseradish peroxidase (anti-HRP) model antibody was used to optimise the parameters, together with the target antigen, peroxidase, in favour of anti-GFAP and GFAP antigen.

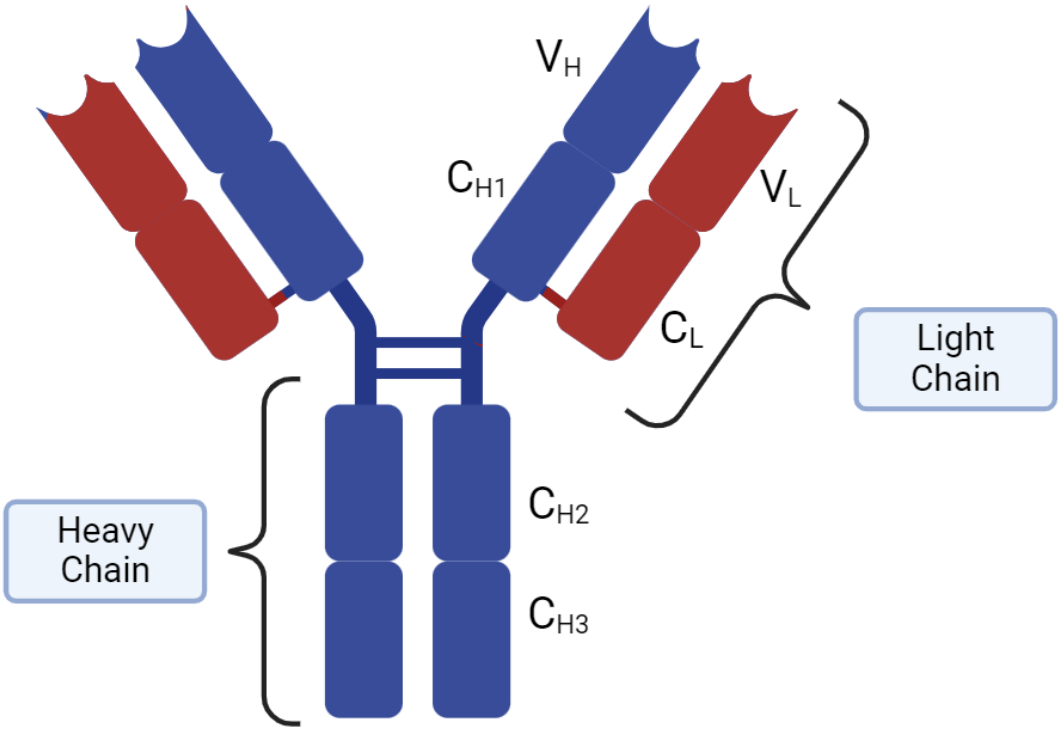

Figure 5- Exemplification of an IgG antibody. This antibody is composed by two regions and 4 polypeptide chains, the heavy chain where it encompasses two 50 kDa segments, and the light chain which encompasses two 25 kDa regions, for a total molecular weight of 150 kDa.
Antibodies also can be separated into their constant region, identified by C_{H1}, C_{H2}, C_{H3} and C_L which do not change amongst the IgG antibody isotype, and the variable region identified by V_H and V_L which are the regions responsible for the identification and binding to target antigens, varying between isotypes to achieve specificity.

1.2.2. Current TBI POC diagnosis methods and Market analysis

Traumatic Brain Injuries Assessment Market was valued at USD 2.9 billion in 2023 and is expected to continue to grow from 2024 to 2032. High market growth can be attributed to the ongoing advancements in diagnostic technologies, increasing incidence of traumatic brain injuries, rising geriatric population, growing number of sports-related head injuries, and escalating healthcare expenditure, among other contributing factors. Moreover, development and adoption of portable and point-of-care diagnostic devices, such as LFAs, are growing. These devices enable rapid, on-site assessment of TBIs, which is particularly valuable in emergency settings, sports fields, and military environments [28].

Currently, in the market, there are only three tools for TBI diagnosis:

- Abbott's i-STAT TBI Plasma Test, a handheld biosensor that detects the TBI biomarkers GFAP and UCH-L1 in plasma to determine the need for further CT scans, with a limit of quantitation of GFAP = 47 pg/mL and UCH-L1 = 87 pg/mL and currently only commercially available POC TBI diagnosis tool in Europe as of 2021, with pending regulatory processes for wider commercial availability in the rest of the markets [29].
- Banyan Biomarkers - Banyan BTI, an ELISA based test which also detects GFAP and UCH-L1 from a blood sample, approved in 2018. [30]
- Biomérieux VIDAS TBI, a benchtop diagnosis test, approved in 2023, also based on GFAP and UCH-L1 which detects and quantifies these biomarkers in a blood sample within 40 minutes, with a decisional cutoff value of GFAP= 22pg/mL and UCH-L1 = 327 pg/mL. This device is also currently on marketed in Europe [31].

With each of these methods, there is either a need for specialized personnel to perform the assays, for example, with the ELISA based test from Banyan Biomarkers or Biomérieux VIDAS' TBI benchtop diagnosis test, or a need to acquire a specialized portable blood analyser for measuring plasma samples, in case of Abbott's method. With the development of easy to use and portable test, as is the case with LFAs, we could strive for faster and cheaper TBI diagnosis, especially in developing countries with less access to these diagnosis tools [32]. This could result in a shift from expensive diagnosis methods to cheaper options, providing easier access for the general population while avoiding unnecessary CT scans or MRIs.

1.3. Raman Spectroscopy

When radiation from the UV to the near infrared (NIR) interacts with a molecule, distinct types of scattering can occur such as Rayleigh scattering, Stokes and Anti-stokes scattering, depending on the energy (hv) with which the photon is released. Out of these types of scattering, Stokes is what matters

the most for Raman spectroscopy as it is more common than Anti-Stokes and shows the inelastically scattered photon with energy hv - ΔE.

Raman spectroscopy works by observing the change in energy between the incident and scattered photons associated with Stokes and Anti-Stokes transitions and measuring the change in wavenumber (cm^{-1}) [33], exemplified in figure 6.

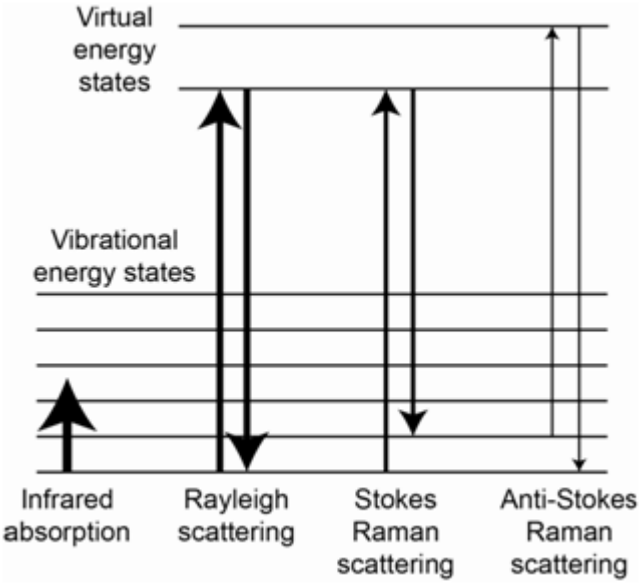

Figure 6- Energy level diagram showing the origin or infrared absorption, Rayleigh scatter, Stokes Raman scatter, and anti-Stokes Raman scatter. Figure adapted from https://chem.libretexts.org.

Since the Raman peaks frequency and intensity are dependent on the vibrational modes, which are characteristic of the bond strength and atoms that contribute to them, this creates a unique fingerprint for each molecule [34], which can be used to identify them in, for example, diagnostics tools, as is the purpose of this work.

Furthermore, usually the frequency of this inelastic scattering is very low, causing the detection of the molecules of interest to be somewhat difficult. It is due to this that another technique was implemented, the surface enhanced Raman spectroscopy (SERS), which combines Raman spectroscopy with nanotechnology and is further explained in chapter 1.5.1 .

1.4. Nanoparticles

As defined by the European Chemicals Agency (ECHA), nanomaterials are chemical substances or materials with particle sizes between 1 to 100 nanometres in at least one dimension. These objects have been used for many years, dating back to the 4th century where these were used to colour ceramics, glass windows and glass cups such as the Lycurgus cup, where a mixture of colloidal gold and silver was used to cause a change in colour when it was illuminated from the inside or from the outside [35].

This unique characteristic is due to the localized surface plasmon resonance (LSPR) phenomenon. When a nanoparticle is irradiated with visible light, the oscillating electrical field causes the electrons to oscillate accordingly, creating an imbalance in charges on the surface of the nanoparticle. This imbalance causes a restorative force to happen, resulting in a well-defined resonance frequency, as exemplified in figure 7. This LSPR directly correlates to the size, also changing with shape change and

material of the nanoparticle, allowing us to cater their characteristics, such as colour, to the necessary use. [36].

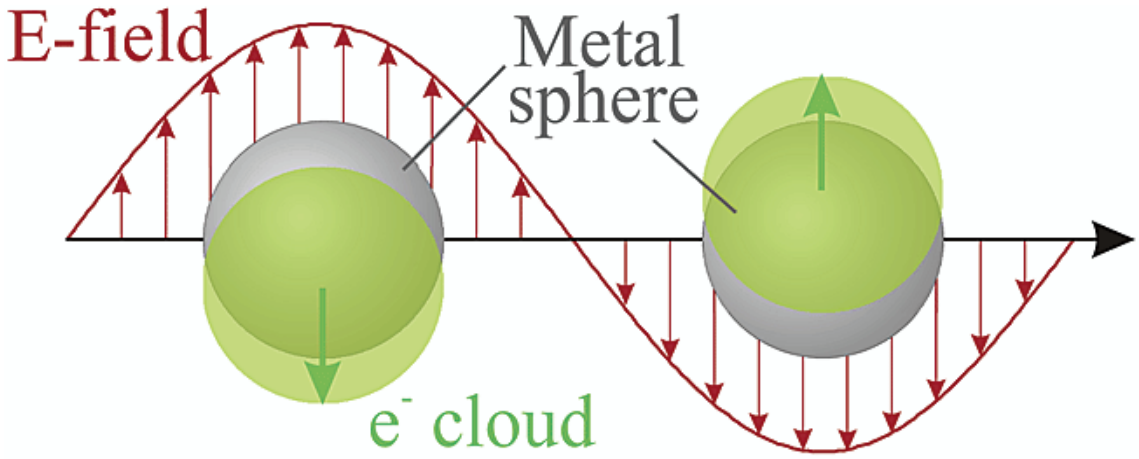

Figure 7 - Plasmon oscillation of the electrons when affected by a NIR light source, causing the displacement of the electrons relative to the nuclei. Figure adopted from K. L. Kelly, E. Coronado, L. L. Zhao, and G. C. Schatz, "The optical properties of metal nanoparticles: the influence of size, shape, and dielectric environment," ˜the œJournal of Physical Chemistry. B, vol. 107, no. 3, pp. 668–677, Dec. 2002, doi: 10.1021/jp026731y.

1.4.1. Gold nanosphere synthesis

For obtaining gold nanospheres (AuNPs), these are most commonly obtained through the "bottom-up" approach, with Turkevich proposing a synthesis protocol in 1951 [37] for the synthesis of AuNPs through the reduction of $HAuCl_4$ with citrate in water. Since then, other authors have tried different approaches, with Ojea Jimenez et al [38] developing a protocol capable of obtaining more finely tuned sized AuNPs by altering the order of addition of the reagents, resulting in smaller AuNPs with a smaller size distribution.

1.4.2. Gold nanoparticle functionalisation and bioconjugation

Nanoparticles, during and after their synthesis, are kept stable by maintaining a negative or positive charge on the surface, given by the surface capping molecules such as citrate, which create a repulsion that stops the particles in solution from aggregating. However, this small size creates high surface energy which creates, in many cases, a non-desirable tendency to aggregate in order to lower this surface energy, leading to a loss of their nanoscale effects [39]. To avoid this, during the synthesis and to maintain their size, molecules such as citrate are added to adsorb to their surface and create a negative energy around these, promoting a repulsion effect between them and delaying their aggregation [40]. However, citrate is not a strong stabilizing agent, needing to be replaced by capping agents such as polyethylene glycol, 11-mercaptoundecanoic acid (11-MUA) or proteins [41]. These serve as stabilizing agents, altering the surface charge of the AuNPs to promote repulsive forces or causing steric hindrance between them.

Gold nanoparticles can be conjugated with a targeting component, such as an antibody, to create a targeted effect. This bioconjugation can be either non-covalent, where the protein passively adsorbs to the surface of the gold nanoparticle through either the charge or the thiol groups, or covalently, where a chemical treatment is applied to bind the conjugating component to the functionalisation agent[42]. Covalent conjugation is usually obtained through the commonly used method of EDC [1-ethyl-3-(3-dimethylaminopropyl) carbodiimide hydrochloride] and sulfo-NHS (N-hydroxy sulfosuccinimide), where EDC is first used to create an amine reactive group, o-Acylisourea, which, due

to its short lifespan and high self-hydrolysis rate, is coupled with SNHS, which reacts with the previous group to create a stable amine-reactive ester, as shown in figure 8.

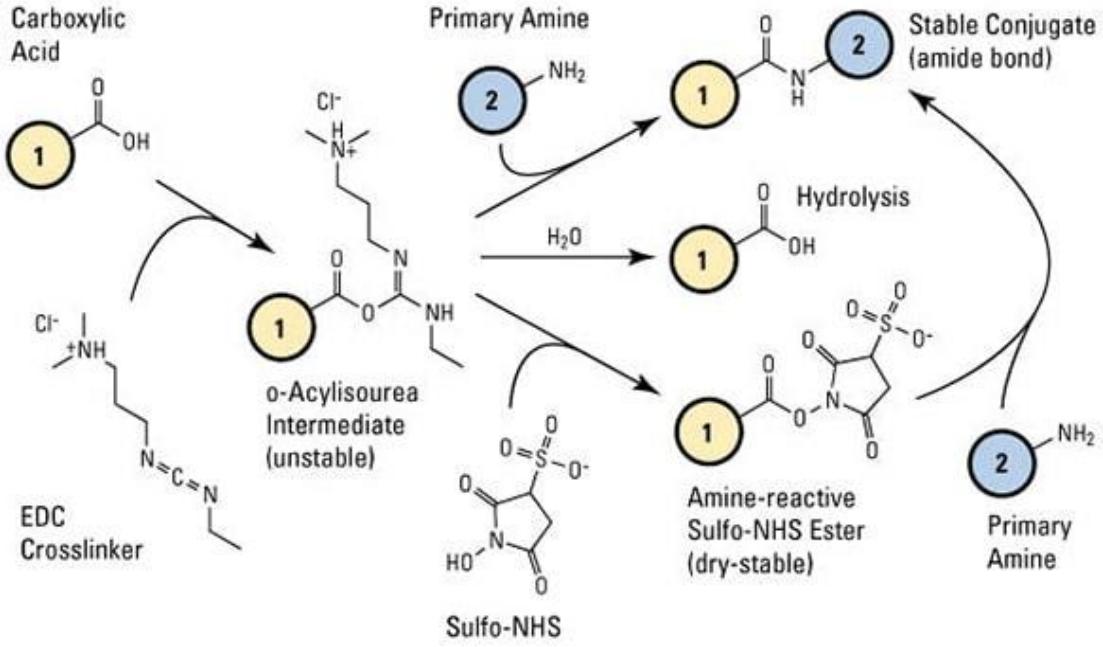

Figure 8 - Bond formation mechanism for the reaction between EDC and SNHS to form a stable amine reactive group. This covalent bonding mechanism enables a stronger and more efficient conjugation than a simpler surface adsorption to a gold surface, in exchange for a higher fabrication cost.

1.4.3. Gold Nanostars (AuNS) and Surface-Enhanced Raman Spectroscopy (SERS)

Gold nanostars are remarkably interesting structures since, not only do they have the typical characteristics of nanoparticles such as the LSPR, the biocompatibility of gold, but they also are synthetised with tips on top to increase the Raman signal of the molecules, enabling SERS detection of analytes in low concentrations.

SERS, much like Raman spectroscopy, is a vibrational spectroscopy technique employed to enable the extremely sensitive detection of analytes in low concentrations, since as previously mentioned, Raman spectroscopy has an inherently weak signal. SERS is a technique which focuses on the enhancement of the signal through two ways: electromagnetic enhancement (EM) and chemical enhancement (CM).

Chemical enhancement happens when there is direct interaction between the adsorbed molecule and the metal surface, resulting in the increase in the Raman cross-section. When adsorbing to the metallic structure, the molecular orbitals of the adsorbate interact with the orbitals of the metal and allow for electrons transfer between these two (a charge-transfer state), effectively changing the electronic band structure of the molecule and making accessible new electronic states. If these new electronic states cause a change in the frequency and it gets closer to the incident laser excitation frequency, the cross-section of the molecule is increased, creating a resonance and increasing the Raman signal [43], [44].

Electromagnetic enhancement is the most common type of enhancement in SERS and usually agreed upon as being the strongest of the two. This enhancement results from the amplification of the Raman signal from the molecule by interaction with the surface under plasmon excitation. When the particle

is much smaller than the incident wavelength, there is a creation of a LSPR, with a unique vibrational frequency. The incident light resonates with the dipole created at the particle and the electrical field intensity of the molecule will be greatly enhanced at that frequency due to the collection oscillation of the SPRs of these metallic particles. This enhancement is stronger at the gaps or junctions of the metal particles due to the creation of “hot spots” which cause a stronger electrical field enhancement, as pictured in figure 9 [45], [46], [47]

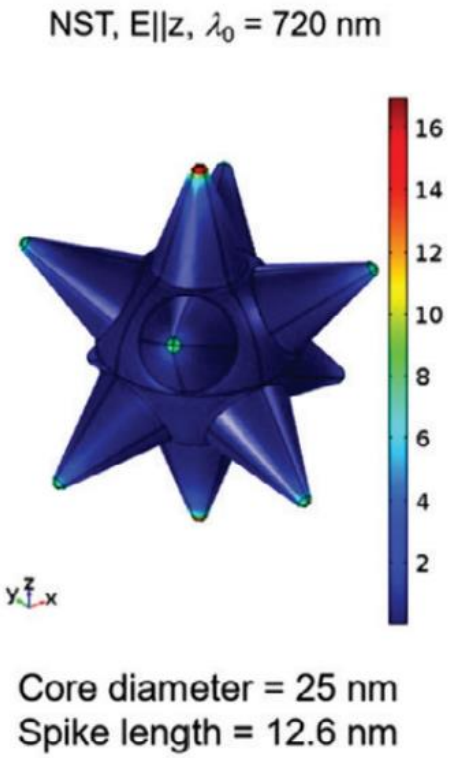

Figure 9 - Local field enhancement maps calculted for a gold nanostar at the maximum SPR intensity, showing an accumulation of energy at the tips of the particle. Figure adopted from Amendola, V., Pilot, R., Frasconi, M., Maragò, O. M., & Iatì, M. A. (2017). Surface plasmon resonance in gold nanoparticles: a review. Journal of Physics: Condensed Matter, 29(20), 203002. doi:10.1088/1361-648x/aa60f3

By employing nanostars in the detection of molecules of interest in low amount, such as is the case for diagnostics tests, the presence of tips on the surface on nanostars causes a hotspot effect, an accumulation of electromagnetic fields which cause an enhancement of the raman signal when in close

proximity of other metallic tips, with an enhancement factor typically around 10^4 to 10^8 depending on the nanostructure [43], [48].

1.5. Surface-enhanced Raman spectroscopy as an ultrasensitive detection technique for lateral flow immunoassay

By combining the ease of use, low development cost and easy storage of a lateral flow immunoassay with AuNSs, we can obtain a faster diagnosis method in a lateral flow immunoassay test and, by combining it with the SERS technique, a higher sensitivity than a normal LFIA can when using the more common AuNPs and other quantitative methods such as colour intensity analysis.

Several authors have developed similar LFIAs, such as Fu, X *et al* [49] for the detection of HIV-1 DNA up to 8 pg/mL, by utilizing AuNP conjugated with complementary HIV-1 DNA using malachite green isothiocyanate (MGITC), or Liu, X *et al* [50] who, with the use of the raman reporter 5,5'-dithiobis-(2-nitrobenzoic acid) (DNTB), managed to develop a LFA with limits of detection of 2pg/mL and 23 pg/mL for two different Sars-CoV-2 proteins.

By using a novel detection method based on 4-mercaptobenzoic acid (Raman reporter) covered AuNS for SERS signal enhancement, we hope to be able to achieve a low limit of detection (LOD) in order to be to enable the use of these tests as a mild TBI diagnostic tool, and avoid the need for CT scans or MRI for every patient in need of these, increasing the speed of patient triage while also lowering the amount of missed diagnosis, as is a common occurrence in the medical field when diagnosing cases of mild TBI.

1.6. Objectives

Traumatic brain injury is one of the biggest causes of brain injury in the world, leading to neurodegenerative diseases like Alzheimer's and cognitive issues. On top of that, mild cases of TBI are missed fairly often, about 8 out of 10 cases [39], leading to possible complications on cases which CT scans or MRI were not able to diagnose. With this in mind, due to its ease of use and no need of trained personnel, the lateral flow immunoassay comes as a good response to the need of a faster method of diagnosis.

By developing a more sensitive way of detecting the biomarker of interest GFAP, through the use of gold nanostars conjugated with anti-GFAP antibodies, coupled with the Raman tag 4-mercaptobenzoic acid to obtain an ultrasensitive, quantitative SERS based TBI analysis (to contribute to diagnosis) diagnosis method, as exemplified in figure 10, we hope to answer the need for a more sensitive method for correctly identifying mild TBI through the use of a sandwich lateral flow immunoassay. Mixing this ultrasensitive method for catching GFAP in blood samples with the ease of use, storage and quickness in getting results associated with lateral flow assays created an optimal platform for TBI diagnosis.

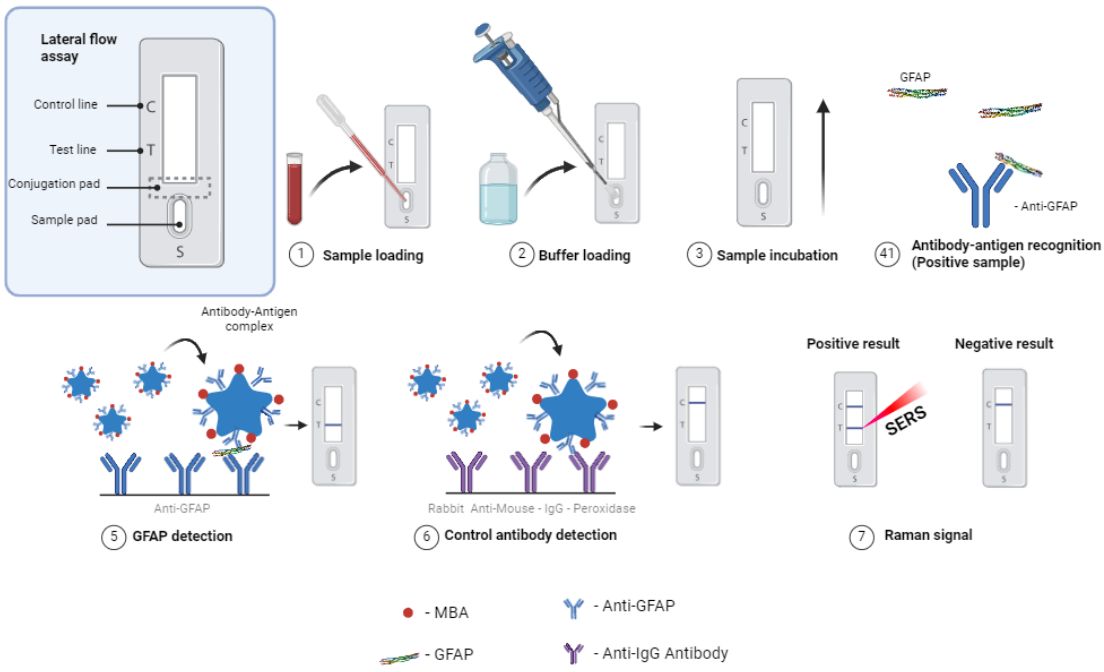

Figure 10 - Schematic for quantitative detection of traumatic brain injury using a lateral flow assay coupled with SERS technology, for a quick and quantitative diagnosis method. Figure made in BioRender

2. Material and methods

2.1. Gold nanosphere synthesis

All glassware and magnetic stirrers used were previously washed with a solution of *aqua regia*, a 1:3 mixture of concentrated nitric acid (65%, Panreac AppliChem, Gatersleben, Germany) and hydrochloric acid (Honeywell Fluka – Thermo Fisher Scientific, Waltham, USA). This mixture allows the dissolution of noble metals and other inert metals, this way avoiding the creation of nucleation points for the growth of nanoparticles [53]. All materials were then washed with ultrapure water until pH 7 was established.

Firstly, we proceeded with the synthesis of gold nanospheres, which was done according to the protocol described by Ojea Jimenez *et al* [38], a modified version of the classic gold nanoparticle synthesis protocol described by Turkevich *et al* [37] to obtain smaller and better size distributed nanoparticles. A volume of 98mL of ultrapure water was added to a 2 necked round bottom flask and put under heating and stirring under reflux to maintain total reaction volume. Next a volume of 2 mL of trisodium citrate (≥ 99%, 343 mM, Sigma-Aldrich, St. Louis, MO, USA) was added to the flask and kept away from sunlight with aluminium foil. After bringing the solution to a boiling, 69.2 uL of a 1.445 M $HAuCl_4$ solution (30 wt. % Au (III) chloride in dilute HCl, Sigma-Aldrich, St. Louis, MO, USA) were added to start the gold reduction reaction. After 5 minutes, the heating, reflux and stirring were stopped so that the reaction could stop and cooled down to room temperature. Finally, the AuNPs solution was filtered by a 0.22 µm syringe filter (GVS North America, Sandford, USA), covered in aluminium foil and stored at 4◦C until further use.

2.2. Bicinchoninic acid assay for total protein determination

The bicinchoninic acid (BCA) assay, first described by Smith et al[54], is a protein determination method based on the reduction of Cu^{2+} to Cu^{+} under alkaline conditions, by interaction with proteins. The created Cu^{+} then reacts with the BCA and changes the previously green coloured solution to an intense purple colour, with an absorbance maximum at 562nm, which can be measured by use of a spectrophotometer. By creating a calibration curve using standard protein solutions, one can obtain the amount of protein present in an unknown recipient. For the standard curve, a protein standard BSA was used (≥ 98%, Sigma-Aldrich, St. Louis, MO, USA) with a series of dilutions of known concentrations, from 0 to 30 ug/ml^{-1}. The working reagent was prepared by mixing 50 parts of BCA solution (Sigma-Aldrich, St. Louis, MO, USA) with 1 part of copper (II) sulphate solution (Sigma-Aldrich, St. Louis, MO, USA). The unknown concentration samples were prepared with dilutions according to the expected values, in this case two dilutions were prepared (1:10 and 1:20). A volume of 10 µL of each solution (standard and unknown) were added in each tube with 1000 µL of working reagent and vortex. These solutions were incubated according to the standard protocol at 37°C for 30 mins. The samples were cooled down to room temperature for 10 min. Afterwards, absorbance at 562 nm was measured for all

the solutions. Through the plotting of BSA standard vs its concentration in $\mu g \cdot mL^{-1}$ it was determined the protein concentration of each unknown sample.

2.3. Gold nanoparticles functionalisation and characterization

To achieve the full coverage of the nanoparticles, these were incubated with 11-mercaptoundecanoic acid (11-MUA) (Sigma-Aldrich, St. Louis, MO, USA) at a molar ratio of 1:2500 AuNPs to MUA, as previously optimised in the lab. For this, the functionalization was performed as follows: first, a solution of 10mM of 11-MUA was prepared in ethanolic solution (≥99%, Honeywell, Riedel-de Haën). The desired amount of AuNP solution was measured, placed on a stirring plate and the correct amount of 11-MUA at 10mM was pipetted as to achieve the 1:2500 molar ratio while stirring vigorously. The solution was allowed to stir for 15 minutes, as to achieve an homogenized solution before being placed at 4°C for 18 hours, as to ensure a complete formation of a monolayer. The solution was then centrifuged at 15000rcfs for 20 minutes in an ultracentrifuge (Beckman Optima LE-80K, California, USA) 3 times, as to remove all excess 11-MUA.

2.4. Gold nanoparticle protein conjugation and characterisation

Due to the difference in morphology and size, gold nanospheres and nanostars need to be handled differently during their conjugation procedures.

Gold nanospheres: For the conjugation of Anti-Horseradish peroxidase antibody (Sigma-Aldrich, Antibody produced in rabbit, P7899) onto gold nanospheres, we started with 11-MUA functionalised, 12nm AuNPs. These antibodies were covalently bound to the carboxyl end of the 11-MUA with recourse to the commonly used EDC-SNHS treatment, where the EDC will react with the carboxyl group, creating the unstable, amine reactive, intermediate o-Acylisourea, which is stabilised by the SNHS, originating a stable, amine reactive intermediate molecule, capable creating a peptide bond with amine groups present in solution. A solution of AuNPs was prepared in MES buffer, at pH 6.5, at 10mM. Next, a fresh solution of EDC and SNHS were prepared in water at 5 mM each and pipetted into the previous solution for a final concentration of 0.06(6) mM and 0.13(3) mM, respectively, as previously optimised in the lab[55]The solution was left incubating for 15 mins on a shaker (Gallenkamp Orbital Shaker Incubator, Cambridge, United Kingdom). After incubation, the solution was centrifuged at 15000 rcfs for 20mins at 4◦C for washing of non-bound EDC and SNHS and resuspended in KPB 2mM, pH 7.4. Afterwards, the optimized amount of protein for full coverage was added for a final antibody to AuNP molar ratio of 50 and left incubating for 1.5h at 4◦C on a shaker. Afterwards, the solution was washed by centrifugation at 9500rcfs, 10 mins at 4◦C , incubated with BSA at a BSA to AuNP molar ratio of 350 for 1.5h on a shaker, at 4◦C. The solution was then washed once more, at 9500 rcfs 20mins, to remove non bound BSA, and resuspended in KPB 2 mM, pH 7.4, ready to be used.

Gold nanostars: For the conjugation of Anti-Horseradish peroxidase antibody onto gold nanostars, we started with 4-MBA(Sigma-Aldrich, St. Louis, MO, USA) functionalised, 60-100 nm AuNSs. These antibodies were physiosorbed onto the AuNSs at a molar ratio of antibody to nanoparticle of 160 by incubating overnight (12-18h) in KPB 2mM, pH 7.4 at 4◦C on a shaker. Next, BSA was added at a molar

ratio of 350 BSA to AuNS and incubated for 1.5h at 4◦C on a shaker. Finally, the solution was centrifuged at 1200 rcfs for 20 mins at 4◦C and storedat the same temperature, ready for use.

2.5. Peroxidase enzymatic activity assay

To confirm the increase in anti-peroxidase antibodies adsorbed or covalently bound to the nanoparticles' surface, these were incubated for 20 minutes with an molar ratio of 5x the previously mentioned optimal antibody to nanoparticle ratio, at 4◦C on a shaker.

Gold nanospheres: After incubation, these were centrifuged at 8000 rcfs for 15 mins at 4◦C and resuspended in KPB 2mM at pH 7.4. This process was repeated 3 times to wash most of the free peroxidase in solution.

Gold nanostars: After incubation, these were centrifuged at 1200 rcfs for 10 mins at 4◦C and resuspended in KPB 2mM at pH 7.4. This process was repeated 2 times to wash most of the free peroxidase in solution.

Next, a protocol adapted from Sigma-Aldrich was employed. A solution of 9.1mM of ABTS was prepared in a solution of 100mM potassium phosphate monobasic at pH 5 and each sample's activity was measured by pipetting 950uL of this solution, 34 µL of hydrogen peroxide at 0.3 % (v/v) and 17µL of the peroxidase incubated bioconjugates. The solution was quickly mixed by inversion and the reaction measured on a UV-Vis equipment (UV-Vis spectrophotometer Cary 50 Bio, Varian®, San Francisco, CA, USA). The reaction of ABTS oxidation, catalysed by the peroxidase, which is characterised by the change in ABTS from light green to dark green, was measured for 3 min at a wavelength of 405 nm, which corresponds to the absorbance maximum of the oxidized ABTS.

To calculate the units of active enzyme, the following equation 4 was used:

$$Units * mg\ solid^{-1} = \frac{(sample\ slope - blank\ slope) * Vf * FD}{\varepsilon * enzyme\ (uL)}$$

(1)

Sample slope – Maximum linear rate

Blank slope – Maximum linear rate of the blank sample

Vf – Final volume in the cuvette

FD – Dilution factor of the enzyme sample

ε – Molar absorptivity for oxidized ABTS at 405 nm, 25◦C = 36.8mM $^{-1}$ * cm^{-1}

2.6. Gold nanoparticle characterization

2.6.1. Colloidal stability

The colloidal stability of both the AuNPs and AuNSs was assessed by increasing the concentration of salt and following the shift of the SPR peak, as well as the ratio between the absorbance at the SPR peak and the absorbance at 600nm for AuNPs and 800nm for AuNSs. The necessary amount of NaCl solution was added to each solution (AuNPs and AuNSs) in order to achieve the following concentrations: 0mM, 10mM, 25mM, 50mM, 100mM, 150mM, 200mM and 250mM for AuNP and 0mM, 40mM, 80mM, 100mM, 150mM and 200mM for AuNSs, to a final volume of 1mL. The effect on both the AuNPs and AuNSs' stability was followed by UV-Vis spectra analysis after NaCl addition, at room temperature.

The AuNPs stability was also assessed by varying the pH of the solution, from 1.6 to 10.8, by addition of 750uL of KPB buffer solution, at the correct pH, to 250uL of AuNP solution, with the effect on the increase of the absorbance at 600 nm, and general loss in absorbance being followed by UV-Vis spectra analysis.

2.6.2. Dynamic light scattering

Dynamic light scattering (DLS) is a technique that is capable of determining the size distribution of nanoparticles in solution by analysing changes in scattered light, while also informing about the sample's degree of polydispersity. Measures were performed in a SZ-100 Nanopartica series (Horiba, Japan) with a 4mW He-Ne laser (532nm) fixed at a 90◦ scattering angle.

The nanoparticle or bioconjugate solution was diluted until it showed little variability between measurements. Each sample was then measured 7 times at 25◦C in a polystyrene, 1mm pathlength cuvette.

Both the Z-Average and peak average were calculated, using the diameter x the frequency for each measure of peak average, with the standard deviation being calculated from these averages.

2.6.3. Agarose gel electrophoresis

Agarose gel electrophoresis is a techniques which consists in separating the samples by size and charge. Agarose gels were manually cast by weighting agarose (UltraPure™, Invitrogen, Thermo Fisher Scientific, Waltham, USA) and mixing it into 1:8x Tris-Acetate-EDTA (TAE) buffer at pH 8, as to obtain concentrations of 0.3% w/v or 0.5% w/v, for nanostars or nanospheres, respectively. This solution was heated up to 85◦C until the agarose was fully dissolved, allowed to cool down for a few minutes until being able to be poured onto a gel tray (mini-sub cell GT, Bio-Rad, Portugal) with a tooth comb. The gel was then placed in the fridge 4◦C to speed up the solidification process for 1 to 2 hours.

When ready, the gel was put in an agarose gel electrophoresis system, immersed in 1:8x TAE buffer at pH 8 and the comb removed.

The bioconjugate samples were centrifuged at 1200 rcfs for 20 mins for AuNS bioconjugates, and 9500 rcfs for 10 mins for AuNPs, the supernatants were discarded, and the samples were resuspended in 10uL of KPB 5mM, pH 7.4 with 15% glycerol. 10uL of each samples were pipetted onto each well and the gel was run at 80V until a good separation of the bands of each well was achieved.

After the run, a photo of the gel was taken and analysed with the ImageJ software (https://imagej.net/ij/), with the most intense pixel being chosen during image analysis.

2.6.4. UV-Vis spectroscopic characterization

The characterisation of AuNPs was through ultraviolet-visible spectra (UV-Vis spectrophotometer Cary 50 Bio, Varian®, San Francisco, CA, USA), which was performed using polystyrene cells with 1cm optical pathlength, in a range of 350 to 700 nm in a UV-Vis spectrophotometer. According to the correlation between the AuNPs diameter and the extinction coefficient ($\varepsilon_{450\ \mathrm{nm}}$) established by Haiss et al. [56], the diameter and concentration of the NPs were determined. This characterisation allows us to analyse the LSPR band of AuNPs which correlates with the colloidal stability, average size and concentration of AuNPs.

According to Haiss et al., it is possible to determine the diameter of gold nanospheres, between 5 and 100nm, based on the ratio between the absorbance maximum (A_{LSPR}) and the absorbance at 450 nm (A_{450}), according to equation 1:

$$Diameter = 0.112e^{2.998*(\frac{A_{LSPR}}{A_{450}})}$$

(2)

With the average diameter of AuNPs determined, the molar extinction coefficient may be calculated for this size through the following equation 2:

$$ln\ \varepsilon_{450} = 3.0869 * ln\ diameter + 10.869$$

With the molar extinction coefficient having been calculated, it is possible to apply the Lambert-Beer[57] equation to calculate concentration of AuNPs in solution.

$$C = \frac{A_{450} * optical\ pathlength * Dilution\ factor}{\varepsilon_{450}}$$

(3)

2.7. Lateral Flow assay

All assays and optimizations were made using nitrocellulose membranes from Advanced Microdevices, India, and all absorption pads were a gentle offer from Ahlstrom, Finland. Both nitrocellulose membranes and absorption pads were cut in 4mm wide strips and turned into dip sticks.

2.7.1. Nitrocellulose membrane selection

The CNPH line of nitrocellulose membranes (mdi Membrane Technologies, India) was selected due to its high adsorption of protein onto the nitrocellulose membrane, allowing for an easier adsorption of the control and test lines onto the dip stick.

Nitrocellulose membrane selection was performed by preparing a 4mm wide dip stick, immobilizing 2ul of 2.2 mg/mL anti-peroxidase antibody and 2uL of anti-IgG antibody onto each membrane to be tested, consisting in CNPH 70, CNPH 90, CNPH 150 and CNPH 200, where the number represent the pore size in µm, and finishing the dip stick with a 4 x 10 mm piece of absorption pad, grade 238 (Ahlstrom, Finland).

2.7.2. Running sample preparation

10µL of the bioconjugates were mixed with the appropriate amount of peroxidase and incubated for 20 minutes. Afterwards, 10µL of the solution were mixed with tween-20 for a final concentration of 0.05% and a PBS, pH 7.4 and BSA solution, for a final concentration of PBS 1x and BSA 1mg/mL.

2.8. SERS measurements

SERS measurements were performed using a Renishaw inVia Qontor micro-Raman spectrometer equipped with an air-cooled CCD as detector and a He–Ne laser operating at 32 mW of 632.81 nm laser excitation. Before each day, the equipment was calibrated using a silicon wafer at 520.7cm^{-1}, the slits were auto-adjusted, and the measuring angle was optimized by auto-adjusting to a gaussian curve. Each sample was focused with either a 20x or 50x Leica objective lens (N Plan EPI) of numerical aperture of 0.12. Single measurements, taken in triplicate on the test line, above and below, with an exposure time of 5 seconds, accumulation time of 7 seconds and laser power of 20%. The data was collected using a WIRE 5.6 software and processed using the same software and the SpectraGryph software, calculating the integral area of the 1587 cm^{-1} line of the 4-MBA, between 1560 and 1590 cm^{-1}.

3.Results and Discussion

3.1. Nanoparticle synthesis, functionalization and characterization

To start working for the LFA final goal, first it was needed to obtain nanoparticles to work with. Two types of nanoparticles were used in this thesis: gold nanospheres and gold nanostars.

In a synthesis, citrate is initially used to regulate the size of the formed nanoparticles , however it is not enough of a stabilizing agent to avoid agglomeration of the nanoparticles, due to them having highly reactive surfaces. Therefore, two capping agents were employed: 4-MBA and 11-MUA, with structures present in figure 11. These adsorb to the gold surface due to the presence of a thiol group, and are used to increase stability by providing a higher charge, promoting electrostatic repulsion between nanoparticles, or causing steric hindrance, making it more difficult for them to win over the repulsive forces stopping aggregation[58], [59]. On top of this, some capping agents may have other functions, such as the 4-MBA, a Raman active molecule which enables the detection of the AuNSs by the Raman signal given, functioning as a label.

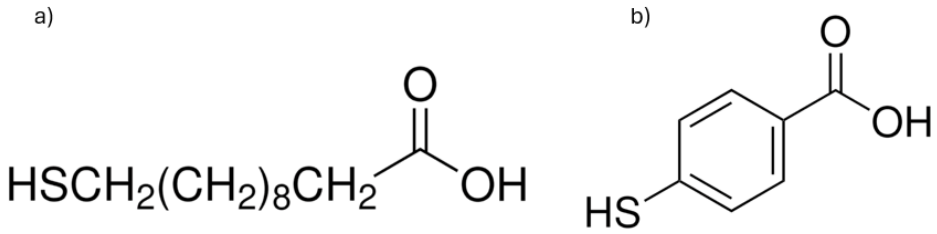

Figure 11 - Molecular structures of the functionalization agents: a) 11-MUA and b) 4-MBA.

For **gold nanospheres (AuNP)**, the protocol used was the one published by Ojea Jimenez et al [38], in order to get better control of nanosphere size when compared to the standard Turkevich approach [37]. The protocol was followed with success, with a visible colour change from yellow, to black and then to red as expected when synthesizing gold nanospheres. For further confirmation of the success of the synthesis, the SPR maximum was assessed by UV-Vis and the size distribution by DLS.

For **gold nanostars (AuNS)**, the synthesis of these was not performed at the Nanobiotechnology lab at Nova FCT, instead they were synthesized and provided by a collaboration with Dr. Maria Enea at the laboratory of Prof. Eulália Pereira, at LAQV/REQUIMTE and the Department of Chemistry and Biochemistry of the Faculty of Sciences, University of Porto, together with their DLS and Zeta potential characterization. These AuNS were also functionalized at the same place, firstly using only 4-MBA and, after noticing low stability when working with these, a 1:1 mixture of 4-MBA and 11-MUA to provide additional stability to these nanoparticles. After arrival, UV-Vis and DLS measurements were taken the same way as the gold nanospheres.~

3.1.1. UV-Vis analysis

Nanoparticles, due to their optical properties related to size, as explained in section 1.4, shown an absorbance maximum ($A_{\lambda LSPR}$) that is characteristic of their composition and diameter. When aggregation occurs, their effective size increases, leading to a loss in absorbance at the initial λ_{LSPR} and

an increase of absorbance at higher wavelengths, called a red-shift [60]. To follow this change, the wavelength of 600 nm was chosen for AuNPs, and 850 nm for AuNSs, based on the previous obtained results. To follow this phenomenon, aggregation was quantified by the ratio of $A_{600}/A_{\lambda LSPR}$ for AuNPs, and $A_{850}/A_{\lambda LSPR}$ for AuNSs.

To assess whether the nanospheres were properly synthesized or not, a UV-Vis spectrum was taken, as shown in figure 12. As expected, the absorbance maximum was around the 517 nm with a well-defined single peak and $A_{600}/A_{\lambda SPR}$ of 0.241, which shows a low absorbance at higher wavelengths than the λ_{LSPR}, indicative of low amounts of aggregation. The LSPR peak was lower than both methods showed in [38], showing that these AuNPs are smaller than the ones obtained by the authors.

According to the equations 1,2 and 3 as described by Haiss et al, we can estimate the diameter and the concentration of the nanoparticles in solution, with the diameter of the nanospheres in figure 8 being of 11 nm.

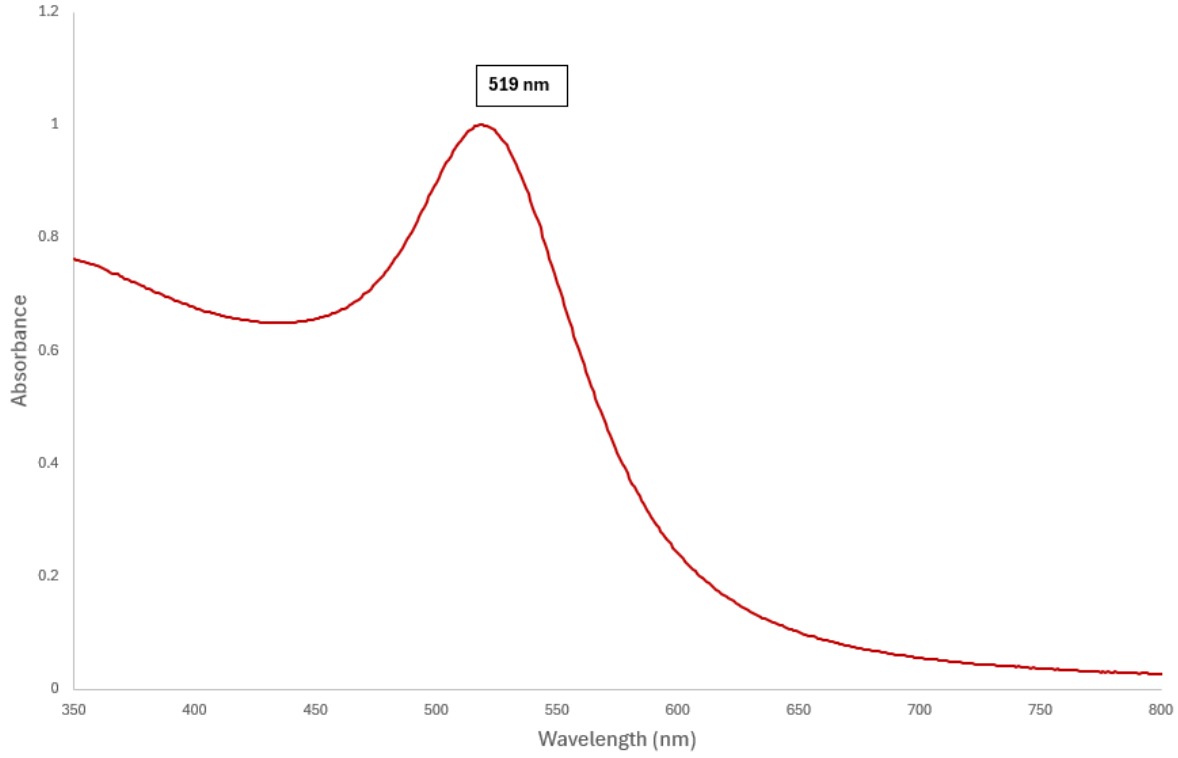

Figure 12 - UV-Vis spectrum of non-functionalized gold nanospheres, with the λ_{LSPR} = 519 nm. It is also possible to conclude that a low number of aggregates were formed by the low absorbance of the nanospheres at higher wavelengths.

The UV/vis spectrum of nanostars functionalized with 4-MBA and 11-MUA, shown in figure 13, reveals a small shoulder at 520 nm, like the λ_{LSPR} of the gold nanospheres. This can be attributed to the core of the nanostars in solution, which also contributes to the higher wavelength λ_{LSPR} [61]. However, as the main difference of the nanostars to the nanospheres, visible in the Uv-Vis spectrum, is the appearance of an λ_{LSPR} at around 811 nm. This is the result of the contribution of the plasmon modes of several tips present in these anisotropic structures, together with the core, which hybridize[62] to form the spectrum shown in figure 13.

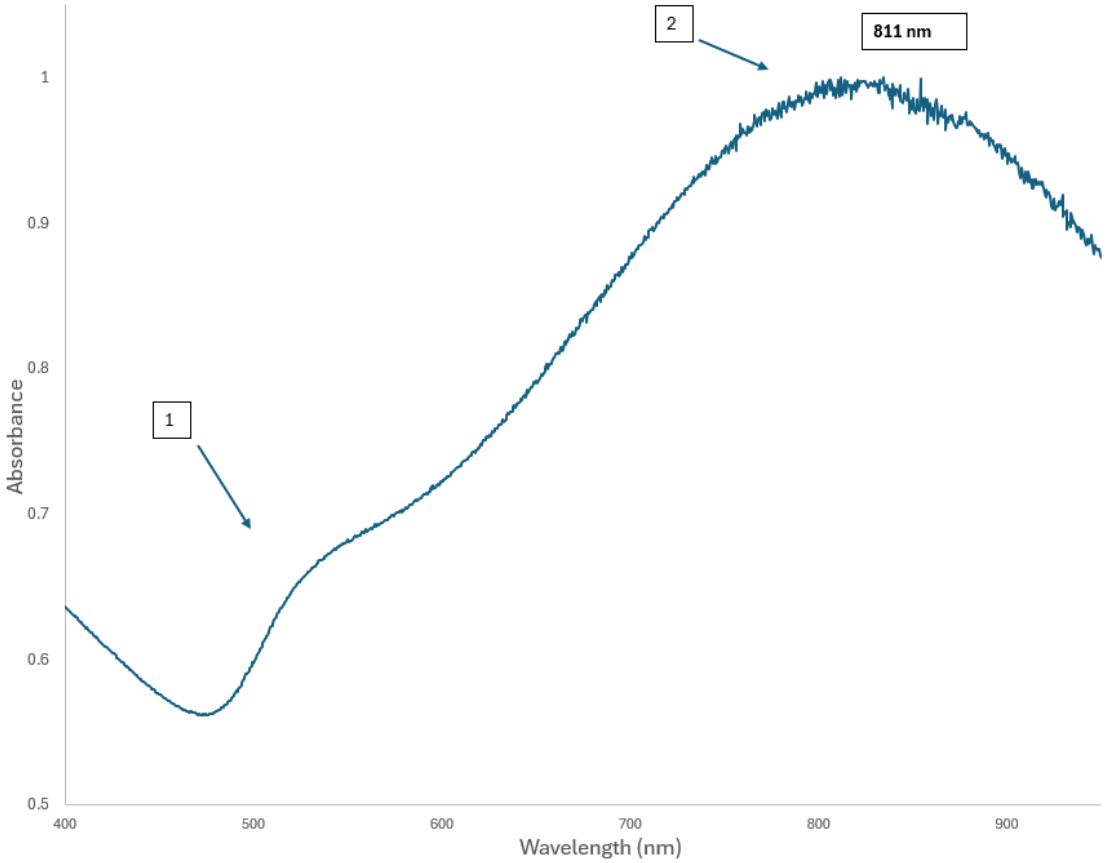

Figure 13 - UV-Vis spectrum of 4-MBA and 11-MUA functionalized gold nanostars. 1- A relative peak at around 520 nm, corresponding to smaller seeds which did not grow to form tips at their surface. 2 - An absolute peak at 811 nm, corresponding to the tipped nanospheres (AuNSs). This LSPR peak corresponds to the sum of the contribution of the core and each different tip on the surface of the nanostar.

As we can see by the spectrum, the λ_{LSPR} at around 811 nm is within the 736-832 nm wavelength range necessary for maximum SERS enhancement for gold nanostars with 8 spikes[61]. With this, the characterization and conjugation were continued to study the stability and formation of the bioconjugates for SERS detection in the LFA format.

3.1.1.1. Functionalization of gold nanospheres

Next, to further increase the stability of the AuNPs, these were incubated with a 11-MUA ethanolic solution. The objective was for the sulphur group of 11-MUA to bind to the gold surface, leaving free carboxyl groups at the AuNP surface, available for the EDC/SNHS covalent bonding step.

The successful functionalization of the nanoparticles was followed by a change in the UV-Vis spectrum, since the replacement of the labile capping agent (citrate) by 11-MUA molecules will cause a change in the refractive index and, consequently, a shift to higher wavelengths [63]. For 11-MUA, the shift is usually around 4 nm for 11 nm gold nanospheres, as previously obtained in works in the same lab, which is in line with the obtained results, shown in figure 14.

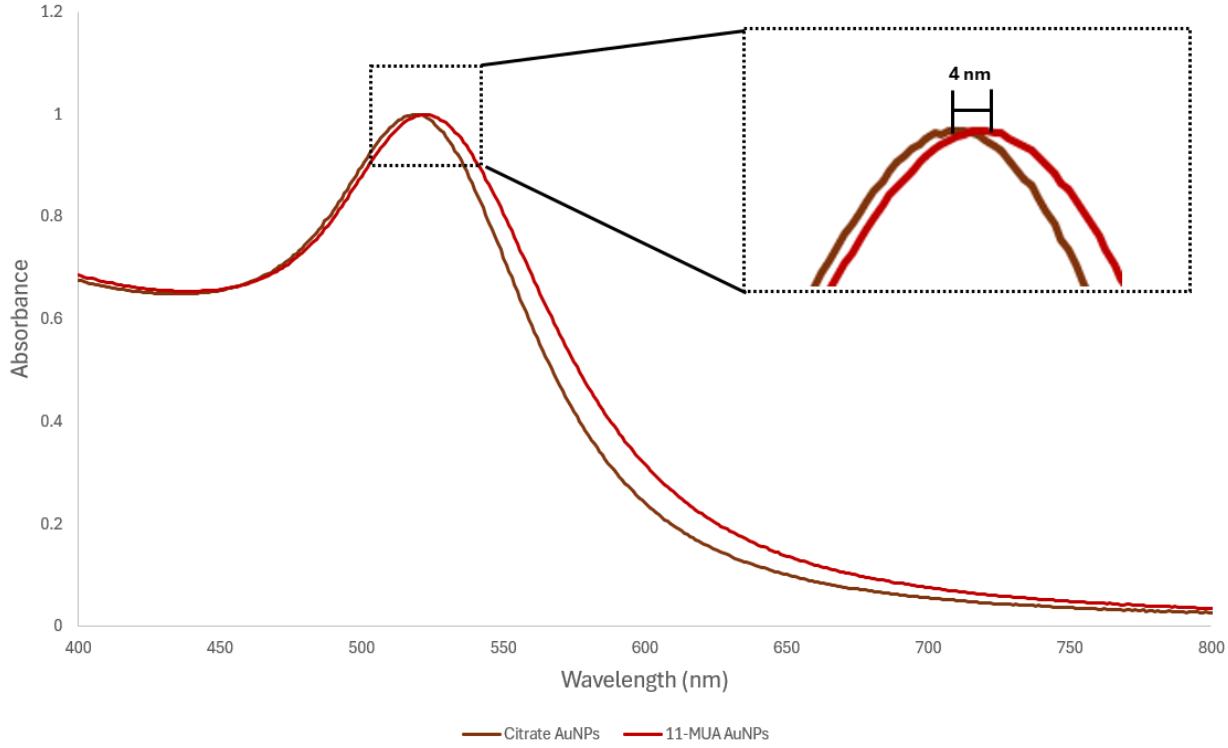

Figure 14 - UV-Vis spectra of citrate capped AuNPs and 11-MUA functionalized AuNPs. A 4 nm redshift can be detected, supporting the replacement citrate by 11-MUA at the AuNP surface.

3.1.1.2. Colloidal stability of gold nanoparticles

To study these nanoparticles' ability to resist aggregation and, therefore, their stability, increasing concentrations of salt were added, and the shift of their size specific LSPR and loss of absorption derived from this redshift was followed by UV-Vis.

Both gold nanospheres (figure 15), and gold nanostars (figure 17) were incubated with increasing amounts of NaCl to assess the degree of colloidal stability of the nanoparticles, measured by the $A_{\lambda LSPR}:A_{600}$ for AuNPs and $A_{\lambda LSPR}:A_{850}$ for AuNSs.

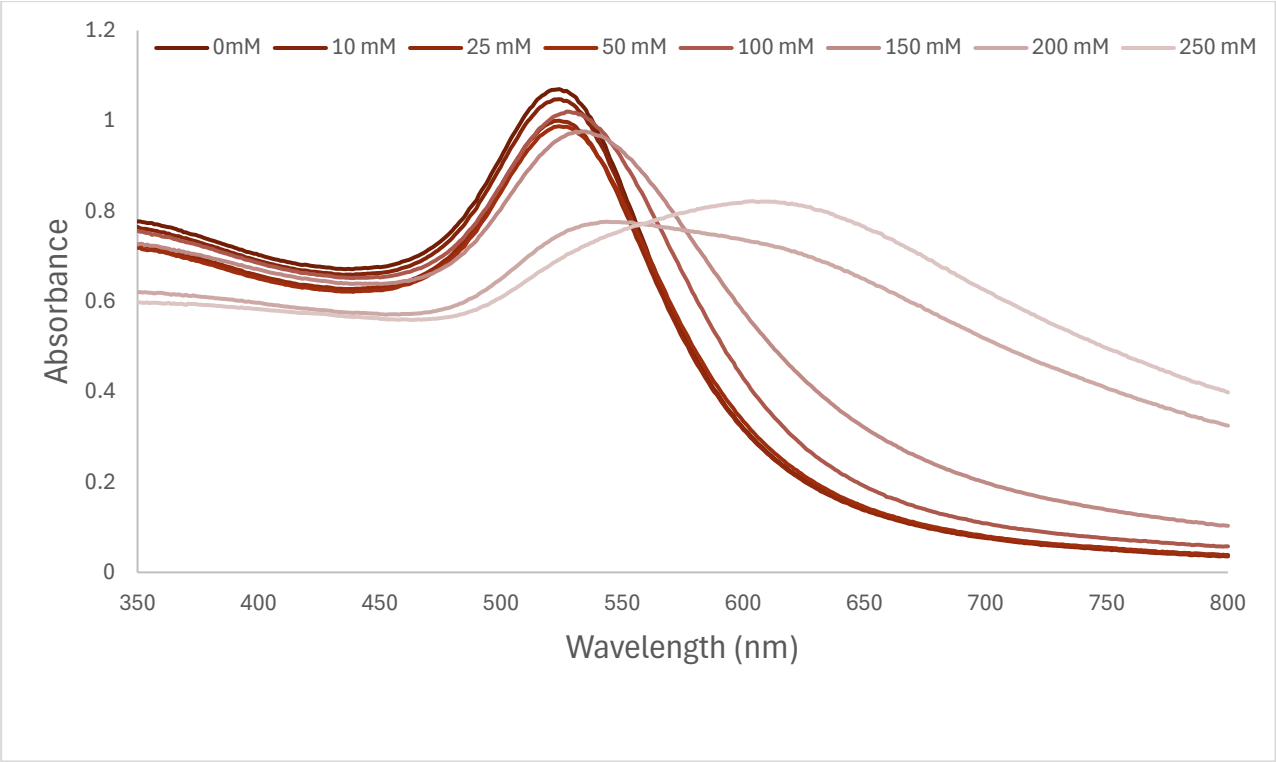

Figure 15 - Evolution of the spectra of AuNPs with the increase of salt concentration, from 0 mM to 250mM. The AuNPs, as seen in the figure, stay stable until 50 mM.

In figure 15 we can see spectra shifting right, as salt concentration increases, an indicator of the increase on size of the nanoparticles derived from the loss of the negative charge, by the addition of salt. In figure 16, aggregation ratios are represented as a function of salt concentration and it is possible to see that the AuNPs stay stable until about 50mM of NaCl concentration, with a slight increase when incubated with the concentration of 100mM, after which the formation of aggregates increases rapidly. This shows a need to stabilize them further since, for the lateral flow assay, the running buffer will be phosphate buffer saline (PBS) with an NaCl concentration of 137mM to avoid non-specific interaction on the test line. The increase in stability will be given by bovine serum albumin (BSA), which will be discussed further ahead.

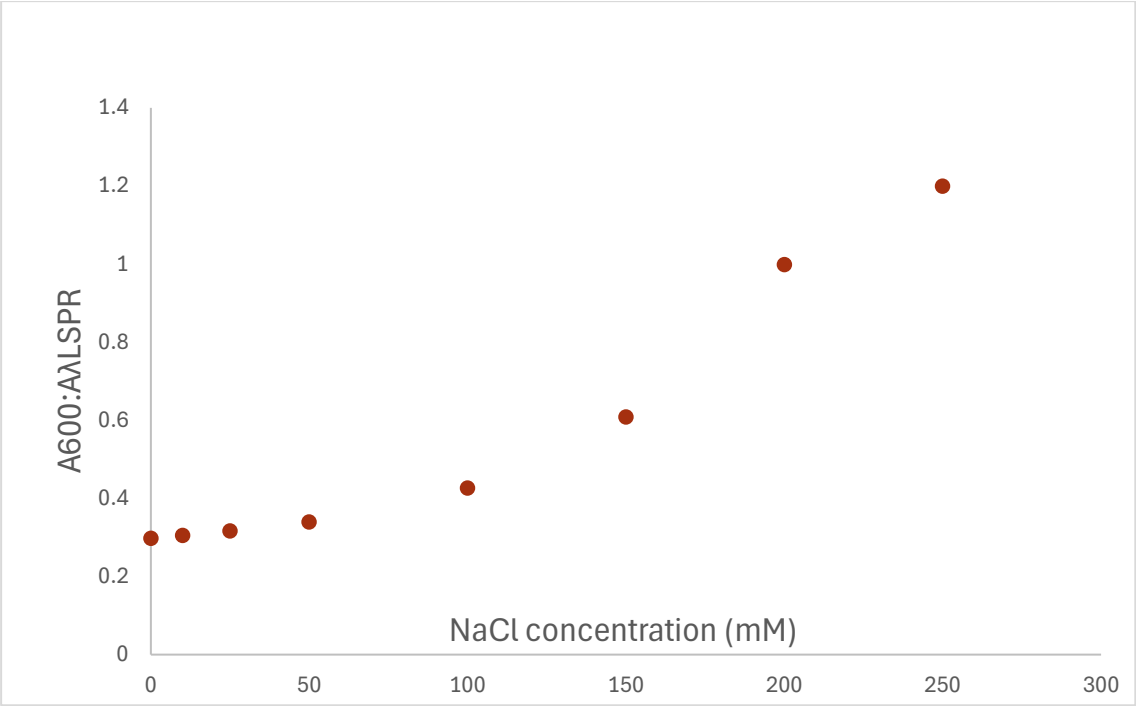

Figure 16 – Aggregation ratio of 11-MUA functionalized gold nanospheres, calculated by $A_{600:}A_{\lambda LSPR}$. The AuNPs remain stable until a concentration of 50-100 mM of NaCl.

The same process to assess colloidal stability was done for AuNS functionalized with 4-MBA. These were incubated with increasing concentrations of NaCl and the resulting decrease in absorbance at the λ_{LSPR} was followed by UV-Vis, with a change in solution colour from a dark blue/black to transparent, signifying a redshift from the λ_{LSPR} to the infrared, as can be seen in figure 17.

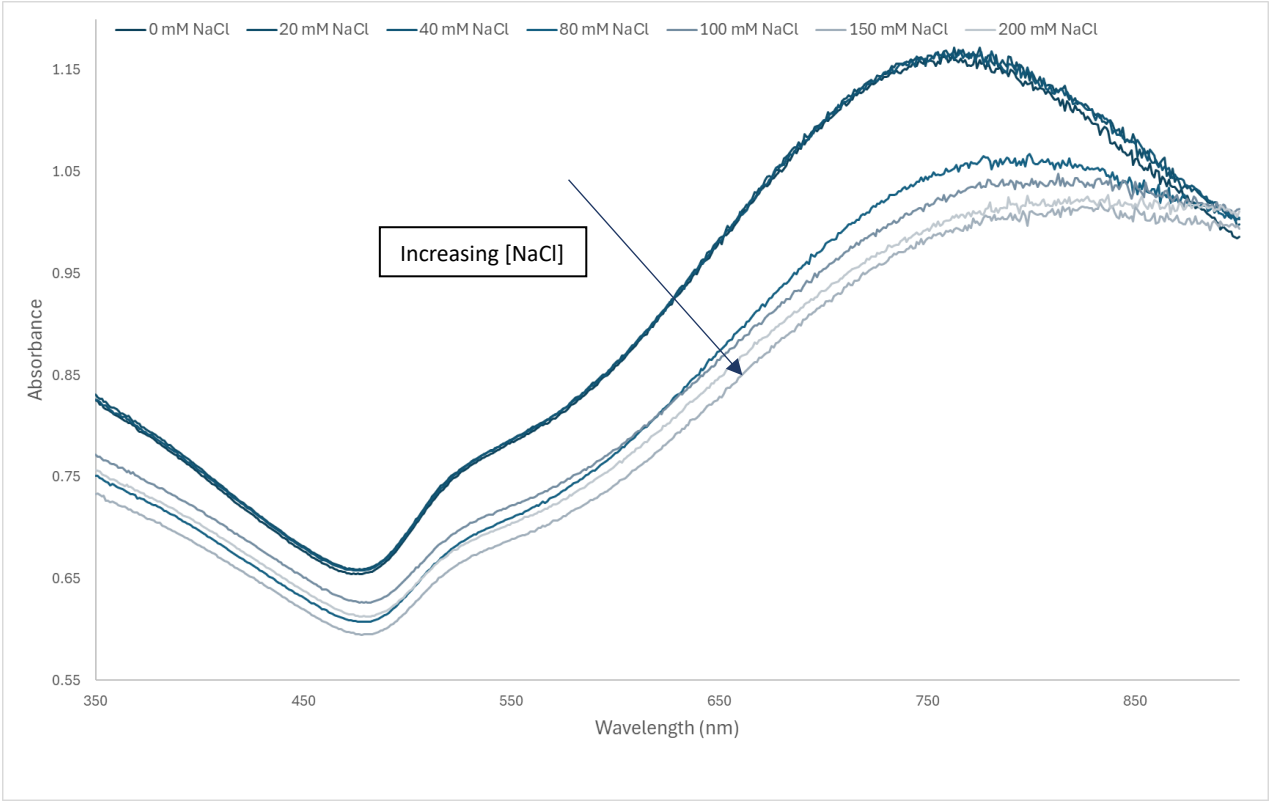

Figure 17 – Colloidal stability of 4-MBA AuNSs, at t=0, with increasing concentration of salt, from 0 mM to 200mM.

By looking at figure 18, it is possible to say that these AuNSs stay stable until a salt concentration of 40 mM, showing to be less stable than the AuNPs at the same salt concentrations. This stability issue was also seen when utilizing other buffers such as KPB at over 5mM would lead to aggregation, leading to difficulties when forming the bioconjugates for the LFA. The stability issues lead to a reformulation of the AuNSs, changing the functionalization agent from 4-MBA to a 1:1 mixture of 4-MBA and 11-MUA, as 11-MUA is a widely used functionalization agent and appears to impart increased colloidal stability to the AuNSs than 4-MBA. This is most likely due to 11-MUA's higher molecular weight (218 g/mol) causing higher steric hindrance than 4-MBA (154 g/mol) capable of aiding the stability of the particles [59], with this mixture being already reported as an aide for stability in enzyme immobilization on AuNPs surfaces [64].

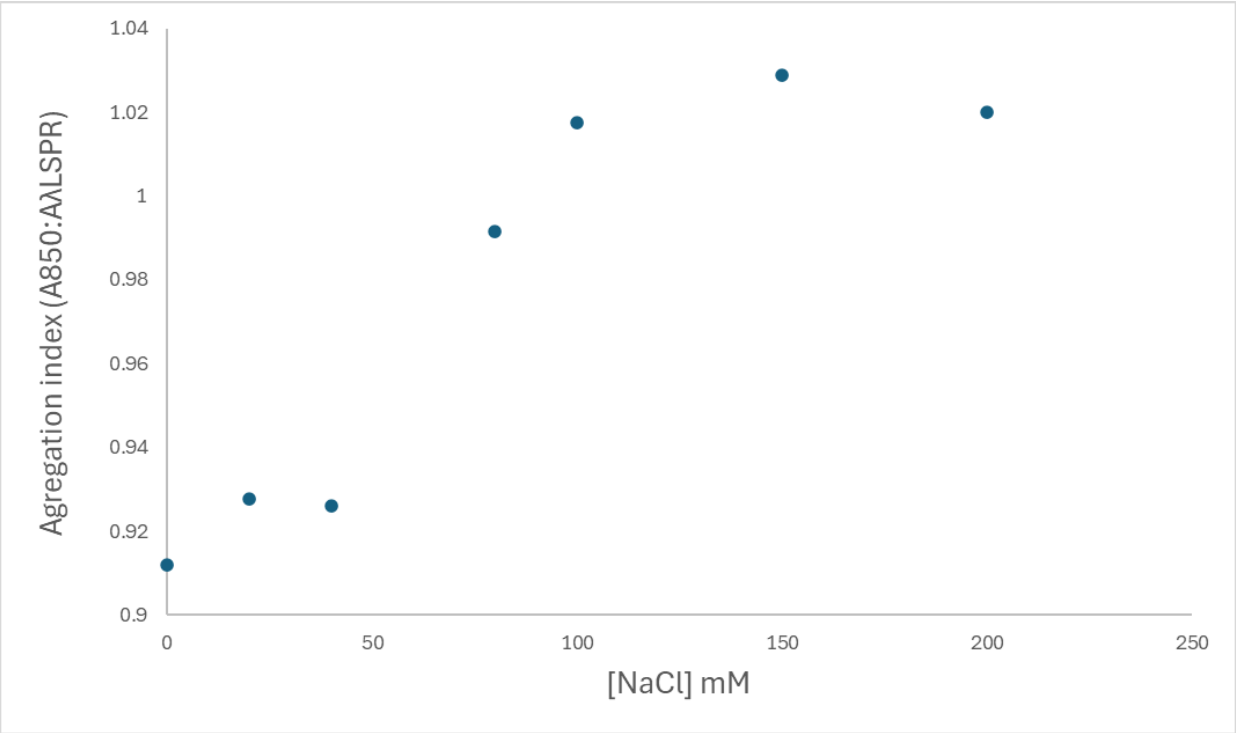

Figure 18 – Aggregation index for AuNSs with increase of salt concentration. It is possible to see that the AuNSs are stable until 40mM of NaCl, where after a big jump happens towards higher aggregation indexes, starting at 80mM of NaCl, indicating a lack of stability at concentrations higher than 40 mM of NaCl.

3.1.2. Dynamic light scattering

To further characterize the synthetized AuNPs and the AuNSs, their size and zeta potential were assessed by measuring on an ELS (Electrophoretic Light Dispersion) equipment.

The average hydrodynamic radius (R_H), calculated by Z-Average, for AuNPs was obtained at 30.5 ± 13 nm as well as a polydispertion index (PDI) of 0.145 ± 0.106. The obtained Z-average size value is higher than the expected size value obtained from the equation for size calculation, proposed by Heiss et al. This size was considerably higher than the average peak size, which resulted in a size of 13.3 ± 2.5 nm, possibly meaning that there are 2 components in play in these measurements, a small and a large one probably composed by non-filtered aggregates, buffer components or specs of dust. This could result in a deviation towards higher values when analysing the sample through Z-average [65]. However, Z-average was continued to be used as it is considered the more robust analysis method (ISO 22412:2017).

The R_H of AuNSs were measured in Porto using a Malvern Zetasizer for an average of 100.65 nm ± 1.26 nm. The zeta potential was measured in the same machine, obtaining a value of -27.9 mV ± 0.65 mV, over the course of 5 measures.
The obtained PDI for the measures was around 0.285 ± 0.004 , which, as mentioned before, is an indicator of some size distribution in the sample. This higher PDI can be attributed to the measure of anisotropic structures that are the gold nanostars, since the difference in number of tips and their size can lead to the increase of the measured polydispersity.

3.1.3. Conjugation of gold nanoparticles

As the final objective of this work is to obtain SERS, which are AuNSs capable of identifying the target antigen in a running lateral flow assay tags to quantitatively and qualitatively identify TBI, these needed to be first conjugated with a SERS active molecule, 4-MBA, a target identifying molecule, the antibody, and a stabilizing molecule which is the BSA, as exemplified in figure 19. At the same time, AuNPs were also treated to achieve the goal of qualitatively identify TBI, as an alternative to AuNSs. For this, each step needed to be studied and optimized to ensure a low cost of the final product.

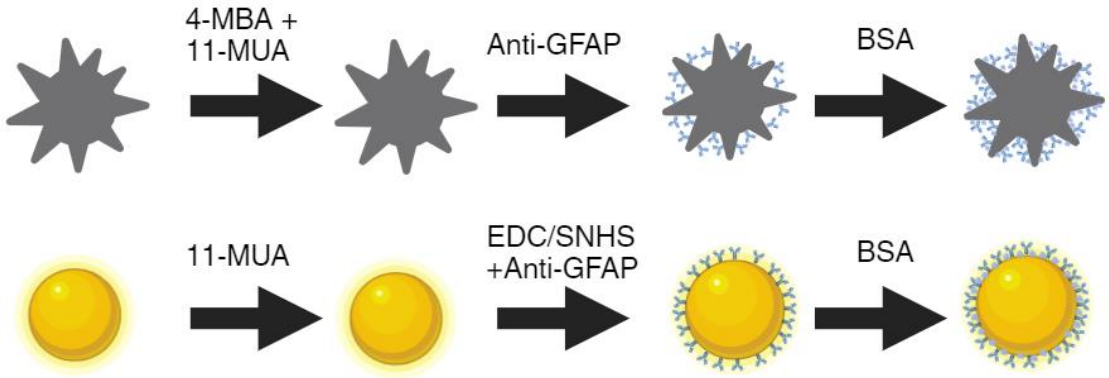

Figure 19 - Exemplification of the steps to develop the SERS tags with the AuNS (top) and spherical probes (bottom) for TBI diagnosis. AuNS (top) were functionalized with both 4-MBA and 11-MUA to obtain a Raman signal and achieve better stability in solution, respectively. AuNPs (bottom) were treated with EDC/SNHS in the second step as to obtain a better retention of the antibodies.

3.1.3.1. BSA conjugation

When running an LFA, the used nanoparticles need to be stable since, if that is not the case, a variety of issues can happen such as the particles not migrating on the nitrocellulose membrane, non-specific signal or other general stability issues. To avoid this, nanoparticles are usually conjugated with stabilizing proteins, usually serum albumin proteins such as bovine (BSA) or human (HSA), or casein. BSA was chosen as it is usually the protein of choice for these assays due to its lower cost and high stability, as seen plenty in the literature [66], [67], [68].
To optimize the amount of BSA needed to be used for both these nanoparticles, these were incubated with the ratios mentioned in the figures 20 and 21 below. BSA was chosen instead of HSA due to the former being less expensive and less prone to interprotein aggregation, favouring a better distribution along the metal surface and decreasing the risk of conjugates aggregation .

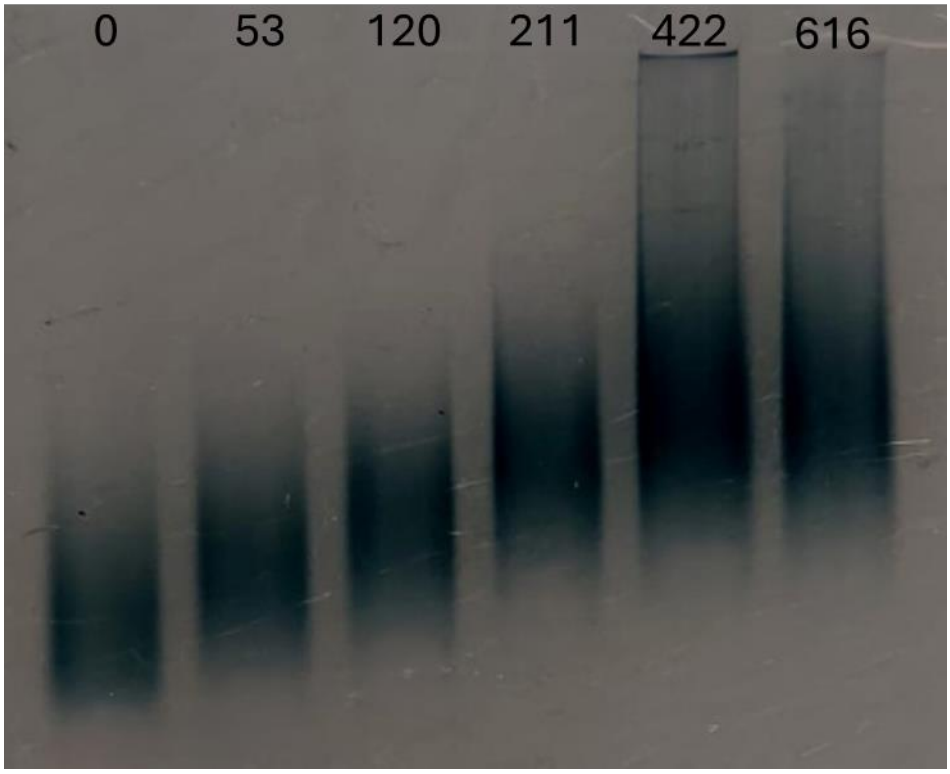

Figure 20 - Optimization of the conjugation of AuNSs with Bovine Serum albumin (BSA). The agarose gel shows the molar ratios of BSA:AuNSs corresponding to each well, increasing from left to right.

To assess the increase in coating of the BSA to the AuNSs, an agarose gel electrophoresis (AGE) was performed. AGE is a useful and studied technique [70], [71] to discern between differently sized nanoparticles due to the increase in size and neutralization of charge, which are caused by the increase in adsorption to the surface of the AuNSs due to the increasingly available protein in solution, causing the decrease in their electrophoretic mobility [72].
Based on the results obtained from the agarose gel, which can be seen in figure 20, the image was analysed using the ImageJ software, selecting the highest intensity areas in each lane, and calculating the electrophoretic mobility following equation 4:

$$\Delta\mu = \frac{v}{E}$$

(4)

Electrophoretic mobility data was fitted to a Hill-type adsorption isotherm (Equation 5) in order to obtain important parameters for data analysis and optimization (figure 21) [73] such as the dissociation constant (K_D), the Hill coefficient (n) and the determination coefficient (R^2).

$$\Delta\mu = \frac{\Delta\mu max * x^n}{{K_D}^n + x^n}$$

(5)

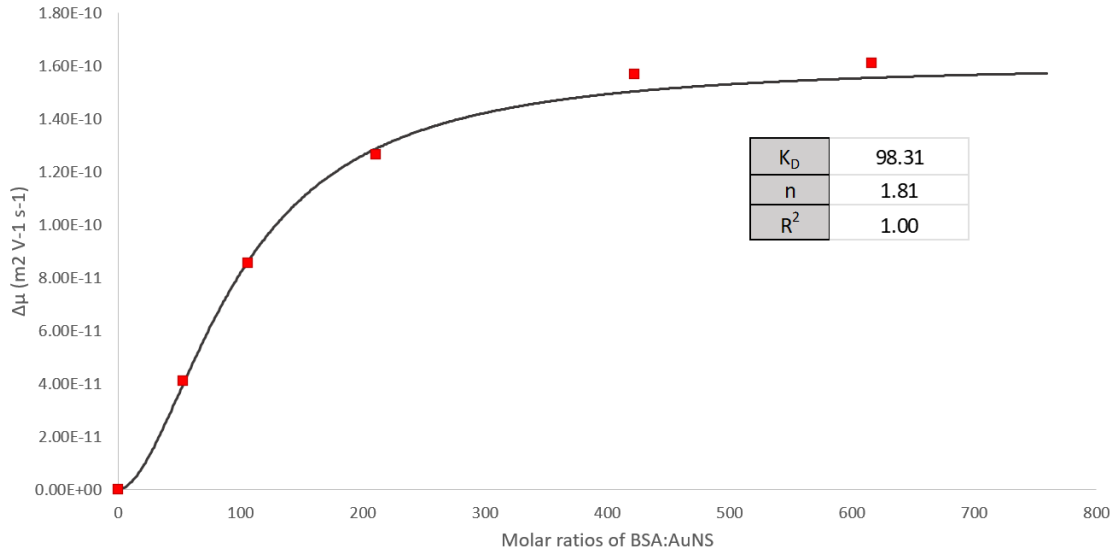

Figure 21 - Fitting of the data obtained in figure 20 to a Hill-type adsorption isotherm. Important parameters such as the dissociation constant (K_D), Hill coefficient (n) and the determination coefficient (R^2) .

For simplicity, all K_D data shown is pertaining to [X]:[Nanoparticle] ratios, meaning that every K_D value is shown as K_D (nM) / [Nanoparticle] (nM), and compared in the same units. The obtained K_D was of 98.31 and the conjugation ratio used to ensure a complete formation of the protein corona was of 350, as the results in the agarose gel showed an intense colour with the ratios of 211 and 422, with the value of 422 showing some aggregation, therefore a midway point was used. It was also possible to obtain the Hill coefficient, n, with a value above 1 (n=1.81). This positive cooperativity indicates an increase in the easiness for the BSA to bind on the surface of the AuNSs as the protein concentration increases, with a value in line with the literature [74] and with previous works in the lab [75]. The choice of a ratio of 350 was made, as this value starts falling in the steady part of the curve, to ensure the highest amount of surface is covered and the AuNSs are as stable as they can be. The amount of protein necessary for a full coverage of the metal surface was around the expected value, according to the previous work [75].

The same process was made for the AuNPs, utilizing the same techniques and methodology as the AuNSs. An agarose gel electrophoresis was performed, obtaining the results in figure 22, where an increase in BSA:AuNP ratio was performed on 11-MUA coated AuNPs, from left to right with ratios of 0, 25, 50, 100, 150, 200, 300, 500 and 750. The results were as expected, with an increase of the size of the AuNPs correlating with the increase in BSA ratio, causing a loss in charge, verifiable by the corresponding decrease in electrophoretic mobility.

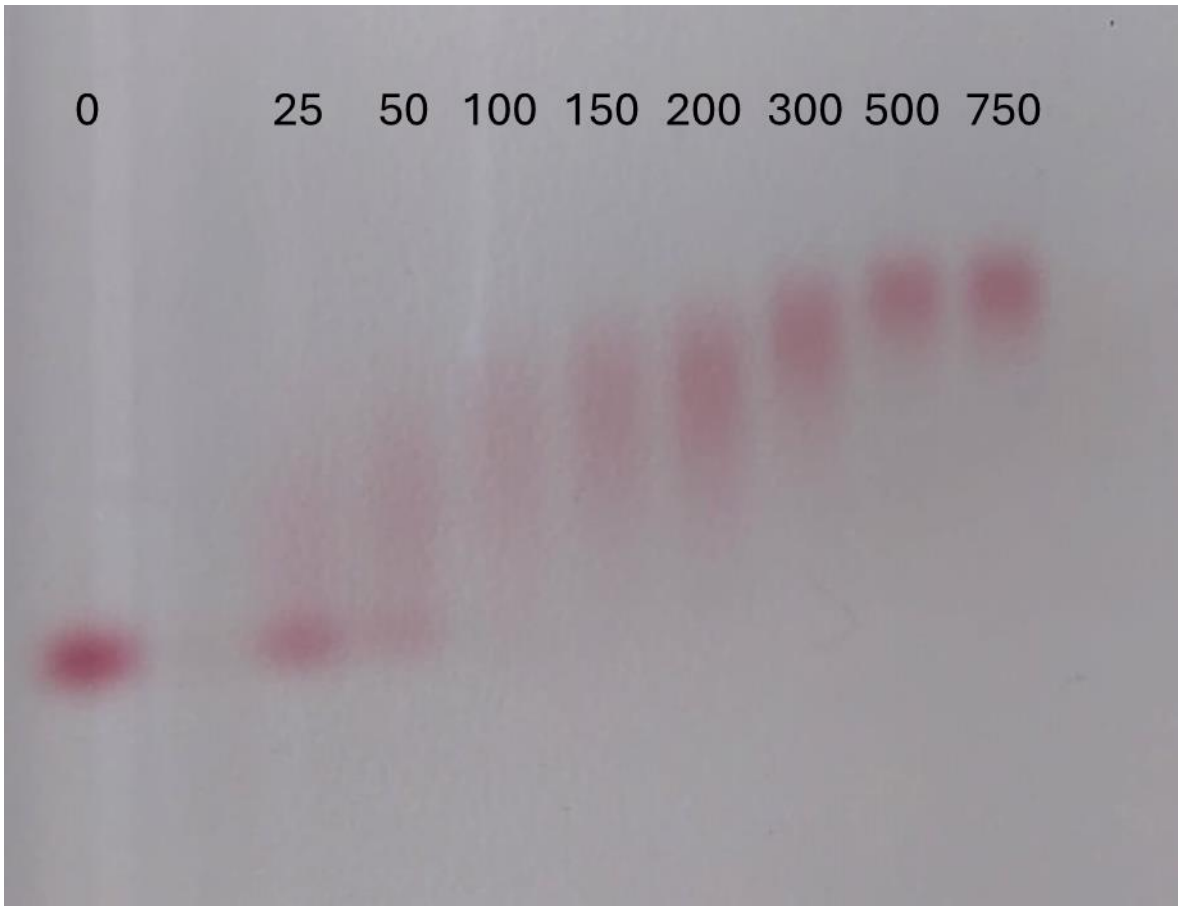

Figure 22 - AGE of 11-MUA coated AuNPs with increasing concentrations of BSA in solution, with the ratios of BSA:AuNP corresponding to each well, from left to right, of 0, 25, 50, 100, 150, 200, 300, 500 and 750, also present of top of each well.

After obtaining the electrophoretic mobility, the data was fitted to a Hill-type adsorption isotherm (Equation 5) in order to obtain important parameters for data analysis and optimization (figure 23) such as the dissociation constant (K_D), the Hill coefficient (n) and the determination coefficient (R^2).
The K_D obtained was lower than the one obtained for AuNS, as expected, since the size of these nanoparticles are almost one fifth of the nanostars, leading to a decrease in surface area compared to these. Furthermore, the Hill coefficient (n = 1.7) obtained indicates a positive cooperativity (n > 1) of the adsorption of the BSA to the AuNP surface, which shows an increase in binding efficacy with the increase of BSA already present at the surface, as already reported in the literature, with citrate capped 60 nm AuNPs presenting an n=1.8 ± 0.7 when conjugated with HSA [74]. However, the Hill coefficient seems to vary from study to study, with citrate capped, 14 nm AuNPs reporting an n=0.6 when conjugated with BSA [66], and an n=0.8 ± 0.3 with polymer coated AuNPs conjugated with HSA, highlighting the complexities of protein surface adsorption. The BSA to AuNP ratio chosen to use as a way to fully coat the nanospheres was of 350 nM, as it already shows little electrophoretic mobility on the AGE and appears on the saturated part of the curve in figure 23.

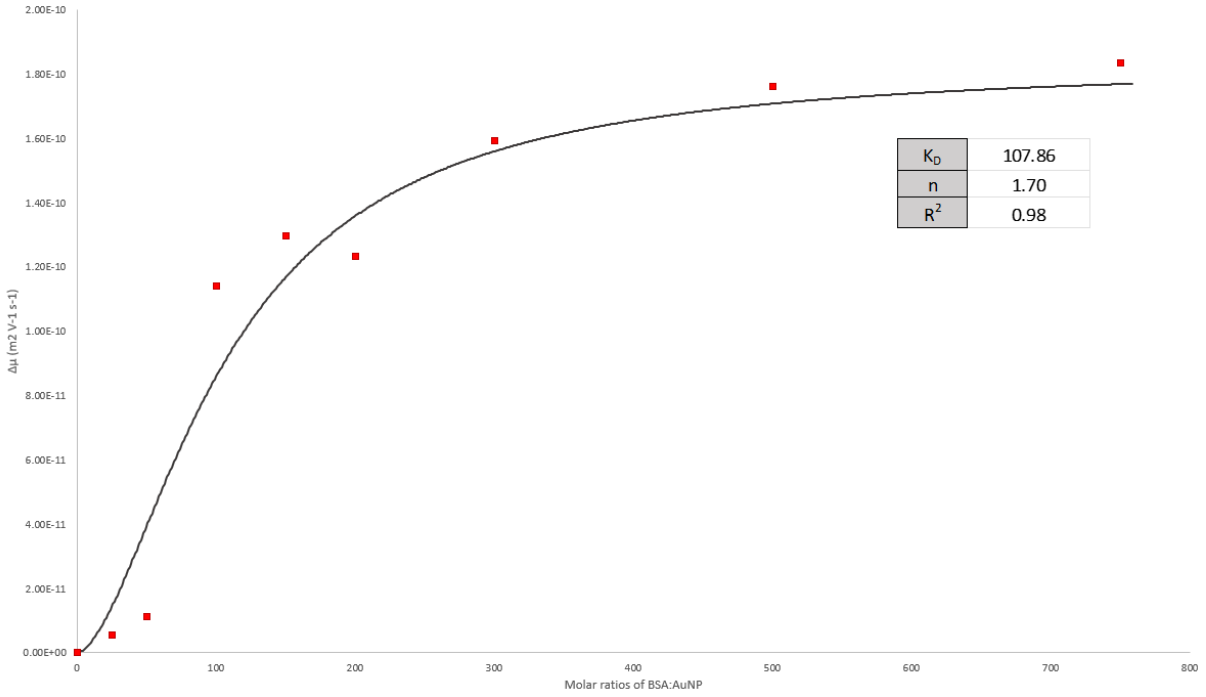

Figure 23 - Fitting of AGE highest intensity points, taken with ImageJ's plot profile, and fitted to a Hill-type adsorption isotherm to obtain the K_D (K_D = 107.86) and n (n=1.7) for the BSA adsorption to 11-MUA functionalized AuNPs.

3.1.3.2. Antibody conjugation

To assemble the SERS tags for the lateral flow assay, the detection part of the tags needed to be tested and optimised. The detection was achieved by conjugating IgG antibodies on the surface of the nanoparticles to achieve specificity to the target molecule, in this case, horseradish peroxidase. Although the final objective of this thesis is to detect the GFAP, due to the high cost of anti-GFAP antibodies and since even the target molecule is a human molecule, this adds to the cost of each assay as the production of a post-translational modified protein requires human cell lines, more specific growth mediums and more specialized techniques which would not be able to be acquired during the time scope of this project.

3.1.3.2.1. AuNP antibody conjugation

For the AuNPs, these were first treated with EDC and SNHS to form a covalent bond with the antibodies, since this method of conjugation wielded better results when tested in activity assays, according to the PhD Thesis from Maria João Oliveira[76], for AuNSs.

To optimize the antibody concentration needed to achieve a full coating of the nanoparticles, these were first treated with EDC and SNHS and incubated with an increasing amount of anti-HRP antibody until no electrophoretic mobility change was observed with the increase in ratio. The resulting agarose gel is displayed in figure 24.

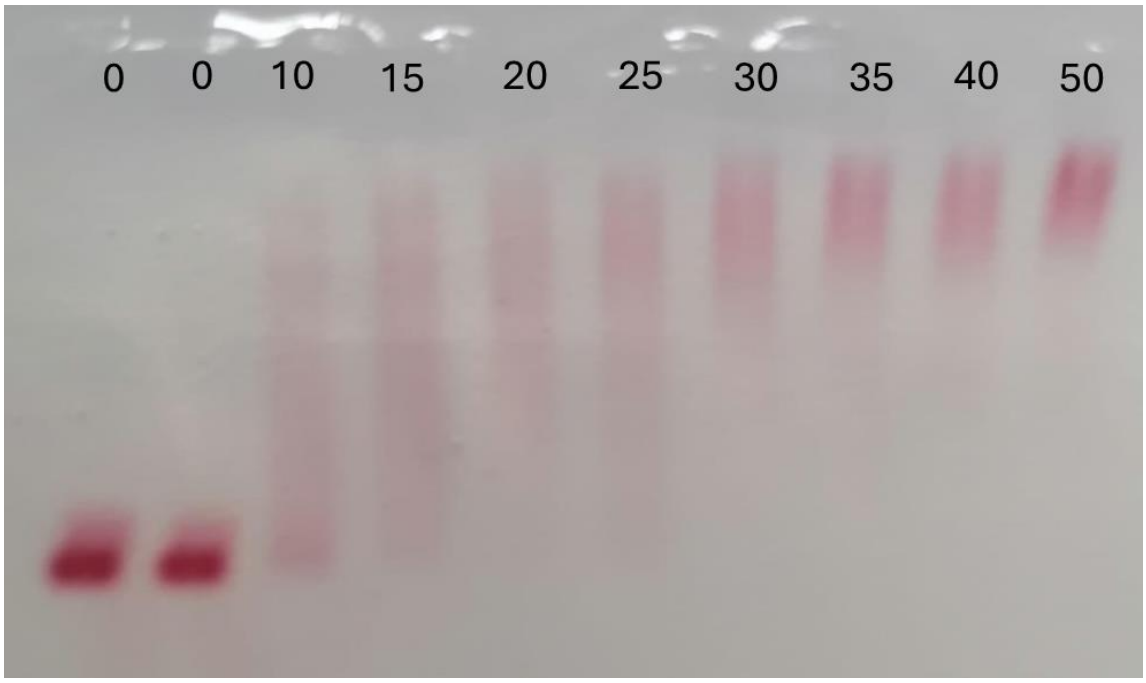

Figure 24 - Agarose gel electrophoresis of anti-HRP antibodies for optimization of the coating concentration. Different concentrations of anti-HRP antibody were tested on each well which are, in order, 11-MUA coated AuNPs, EDC/SNHS treated 11-MUA AuNPs, anti-HRP:AuNP ratio of 10, 15, 20, 25, 30, 35, 40 and 50.

The agarose gel electrophoresis (figure 24) was analysed with ImageJ software, the highest intensity spot was selected in each lane, and electrophoretic mobility was calculated and fitted to a Hill-type adsorption isotherm, obtaining the K_D, n and R^2 (figure 25). The affinity constant came to a value of 17.3, which is in line with other works in the literature [74], and a cooperativity parameter value of 4.24, showing a positive cooperativity (n > 1) which is also present in the literature [74] although with a value 2 units lower than the one obtained here. This could be due to the lower concentrations of antibody used in the incubations, which could incur in error, or due to the way the antibodies adsorb to the AuNPs, not being in enough concentration to populate all nanoparticles equally and creating a more intense non-populated band in the agarose gel which does not fully correspond to the AuNPs distribution.

The conjugation ratio chosen for further work was of 50, since an increase in the intensity of the colour in figure 24 can be seen from ratios 30 to 50, with 50 showing the highest intensity.

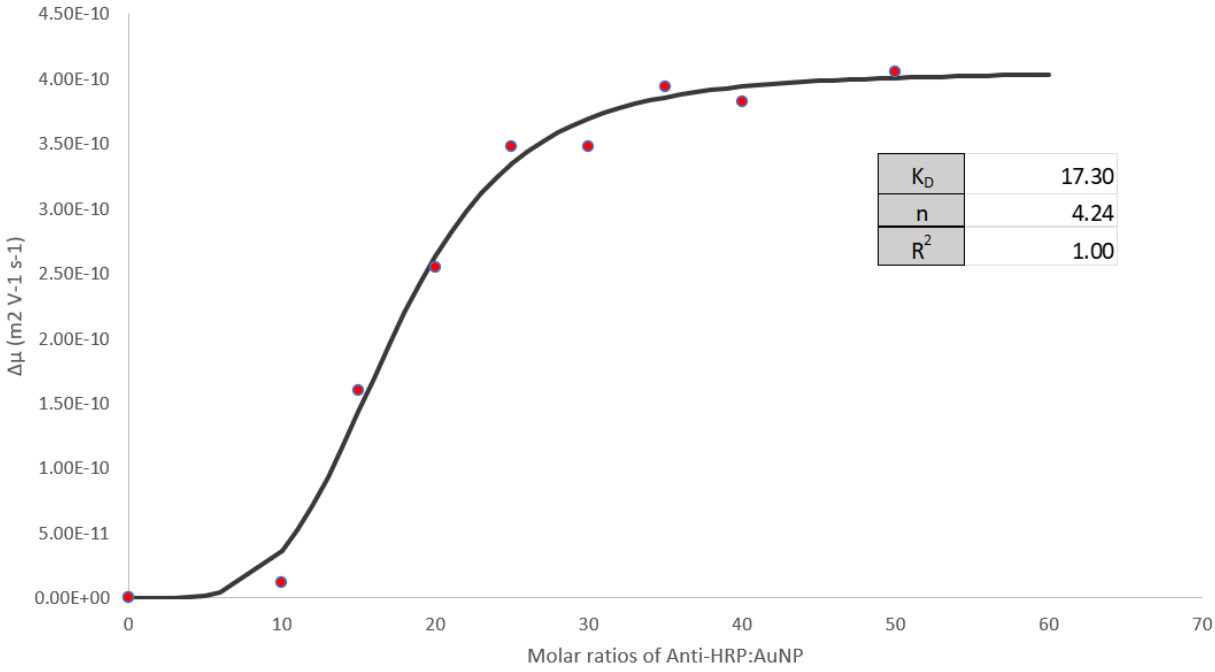

Figure 25 - Electrophoretic mobility of AuNPs with increasing concentration of anti-HRP antibodies, fitted to a Hill-type adsorption isotherm. The experimental results are highlighted as red circles, and the fitting is highlighted as the black coloured sigmoidal curve. Important parameters were able to be obtained such as the K_D = 17.3, and an n = 4.24.

With the BSA protein and antibody ratios studied and optimized, the full bioconjugates were assembled. To follow the formation of these bioconjugates, the process was studied by UV-Vis. As the size of the nanoparticles grows, the absorption maximum drifts shifts the LSPR of the nanoparticle to a higher wavelength since the addition of substances on the surface, namely proteins and the 11-MUA functionalisation agent, cause a change in the local refractive index, reported consistently in the literature [77], [78]. Therefore, the step-by-step formation of the AuNP bioconjugates and respective LSPR red-shifts, may be observed in figure 25.

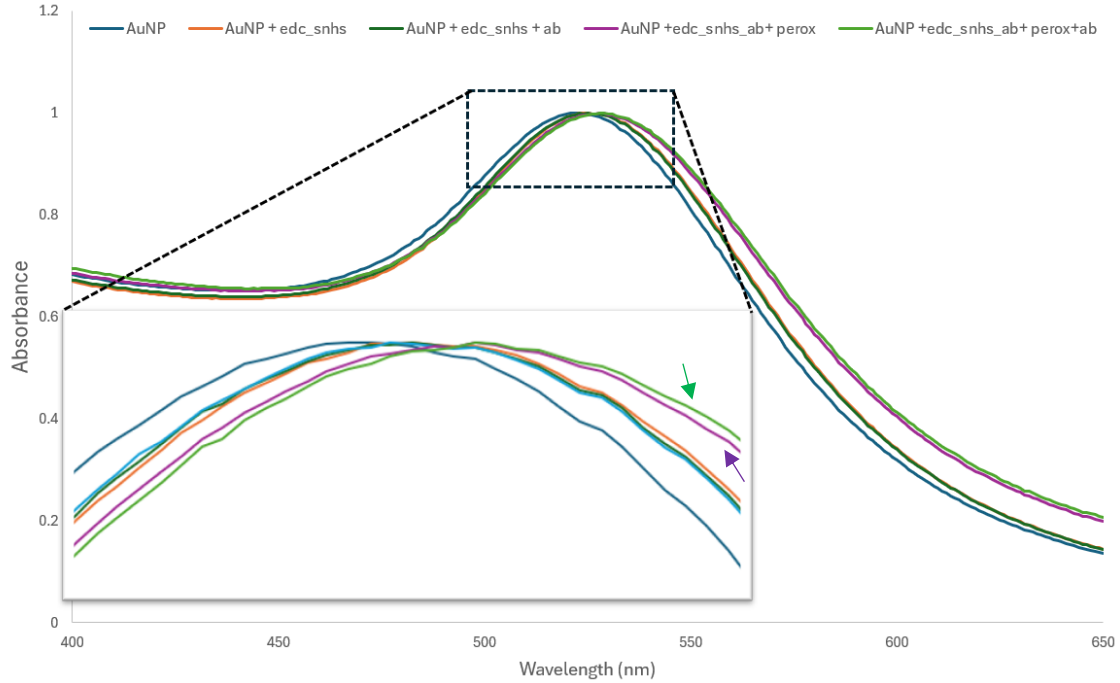

Figure 26 - Uv-Vis analysis of the conjugation process of AuNPs for the formation of bioconjugates. The figure shows a red-shift of the spectra as the AuNP radius' increases, starting with the 11-MUA capped AuNPs and ending with the full bioconjugate formed by the AuNPs treated with EDC and SNHS, conjugated with anti-HRP antibody, followed by BSA, peroxidase, and finally another anti-HRP antibody incubation to simulate the full sandwich happening in the LFA. No shift from the full bioconjugate with the peroxidase to the full "sandwich" was observed from the purple line to the faint green, indicated with a purple and green arrow, respectively.

Lastly, a DLS measurement was made for each step of the conjugation of the AuNPs to follow the formation of the full bioconjugate.

Table 1 – Z-Average DLS measurements results of the formation of the AuNP bioconjugates, with the analysis of each of the conjugation steps. "F" indicates functionalised bioconjugates, with 11-MUA.

	Size (nm)	PDI
AuNP	30.5 ± 13	0.145 ± 0.106
$AuNP_F$ + Anti-HRP antibody	77.6 ± 12.6	0.078 ± 0.080
$AuNP_F$ + Anti-HRP + BSA	74.2 ± 11.6	0.189 ± 0.135
$AuNP_F$ + Anti-HRP + BSA + HRP	132.6 ± 14.5	0.213 ± 0.150
$AuNP_F$ + Anti-HRP + BSA + HRP + Anti-HRP	279.1 ± 55.8	0.112 ± 0.051

The results obtained indicate an increase in size, as expected, with the addition of each component. By analysing the PDI, it is possible to assess the degree of polydispersity of the sample, with values closer to 0 signifying that the sample is monodisperse, and closer to 1 being polydisperse[79]. With this, we can see that the samples are mostly monodispersed, with some having higher values of PDI, such as the AUNP+Anti-HRP+BSA+HRP sample with a PDI of 0.213 ± 0.150, possibly most likely caused by an

uneven distribution of the enzyme over the bioconjugates. This can also be seen after the addition of the second anti-HRP antibody, leading to a large size deviation (55.8 nm) possibly caused by an uneven distribution of these by the bioconjugates.

3.1.3.2.2. AuNS antibody conjugation

Initially, the same protocol was followed as Maria Joao Oliveira [76] using covalent conjugation to increase the activity of the conjugates, however, these could not be achieved as every time these were attempted, it would result in aggregation, making it impossible to optimize antibody ratios or BSA ratios. Since not using this chemical treatment would lower the cost of the assay in exchange for lowered sensitivity, we proceeded with the physisorption method until the lateral flow assay signal optimization, where it would be seen if there is a need to increase the limit of detection

The same optimization steps of the AuNPs were performed for the AuNSs, to obtain the optimal amount of anti-HRP antibody to fully coat them (figure 27).

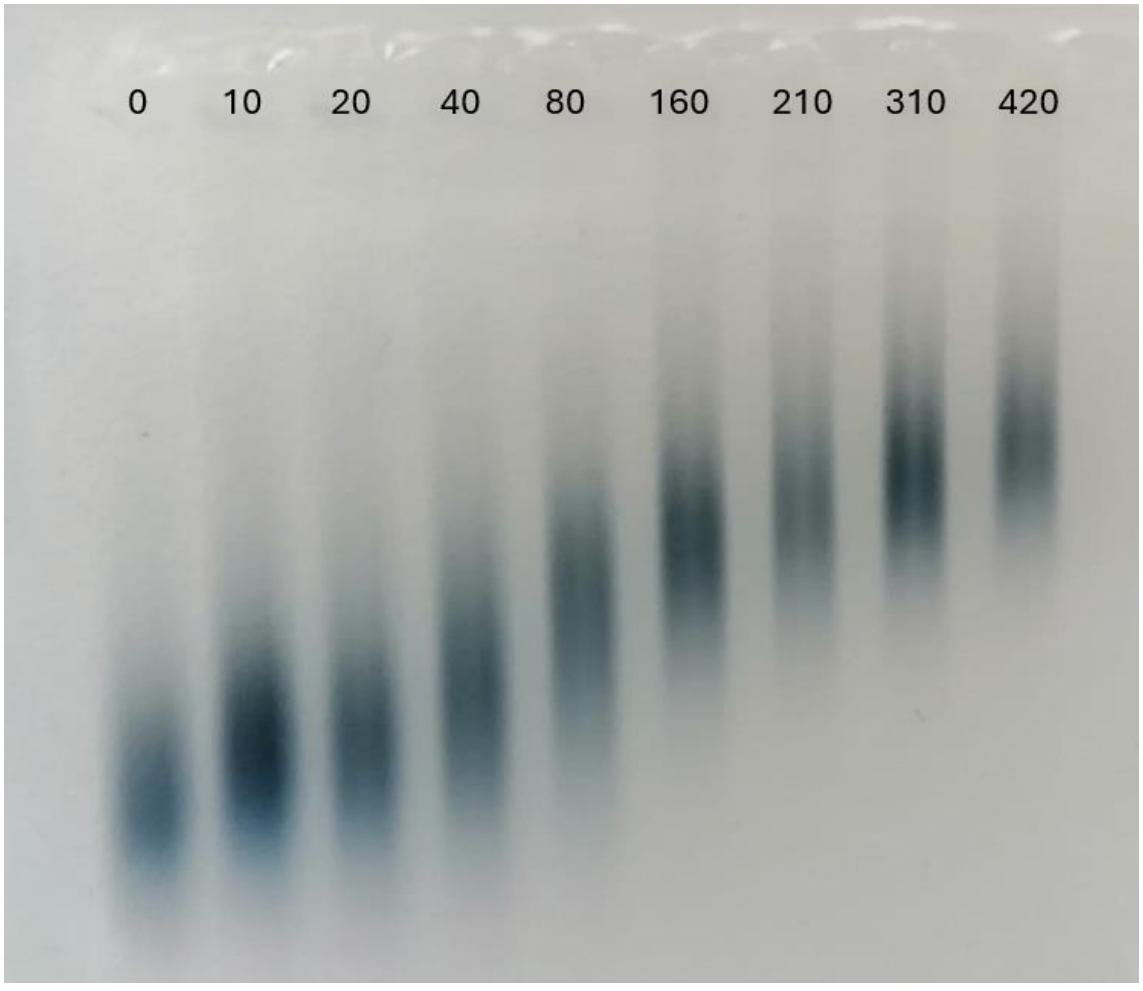

Figure 27 - Agarose gel electrophoresis of AuNSs incubated with anti-HRP antibody. The identified wells' anti-HRP:AuNS ratios are, in order: 0, 10, 20, 40, 80, 160, 210, 310 and 420 with AuNSs at a concentration of around 0.2 nM.

The obtained agarose gel electrophoresis results were analysed with the ImageJ software, where the highest intensity point was selected, and the electrophoretic mobility was calculated and adjusted to a Hill-type adsorption isotherm (figure 28).
A positive cooperativity parameter was obtained (n=1.34) showing an increase in easiness of binding

to sites on the surface of the AuNSs as the antibodies continue to bind to it. This correlates positively with the literature, with some reporting neutral cooperativity (n=1) (70 nm gold AuNSs) [80] and positive cooperativity (n=2) (60 nm AuNPs) [74], however the complexity of protein adsorption to surfaces due to the localized different domain charges (especially in larger proteins like IgG antibodies), steric hindrance and medium pH which all change the way proteins adsorb to surfaces, being necessary a more in depth analysis of these mechanisms to obtain a more accurate picture [81]. The binding affinity value obtained was of K_D = 59.20, which is lower than the one obtained with a very similar type of bioconjugates by Oliveira et al[76], with a K_D value of 190. This change could be due to differences in the synthesis of the AuNSs, namely the change in functionalization, where a 1:1 mixture of 11-MUA and 4-MBA was used here whereas solely 4-MBA was used by Oliveira et al., contributing to charge changes which may result in the decrease of the adsorption capability of the IgGs. The chosen Anti-HRP to AuNS ratio was of 160 nM as it already appears on the saturated part of the curve in figure 28, and shows good stability when centrifuging the samplechanges which may result in the decrease of the adsorption capability of the IgGs.

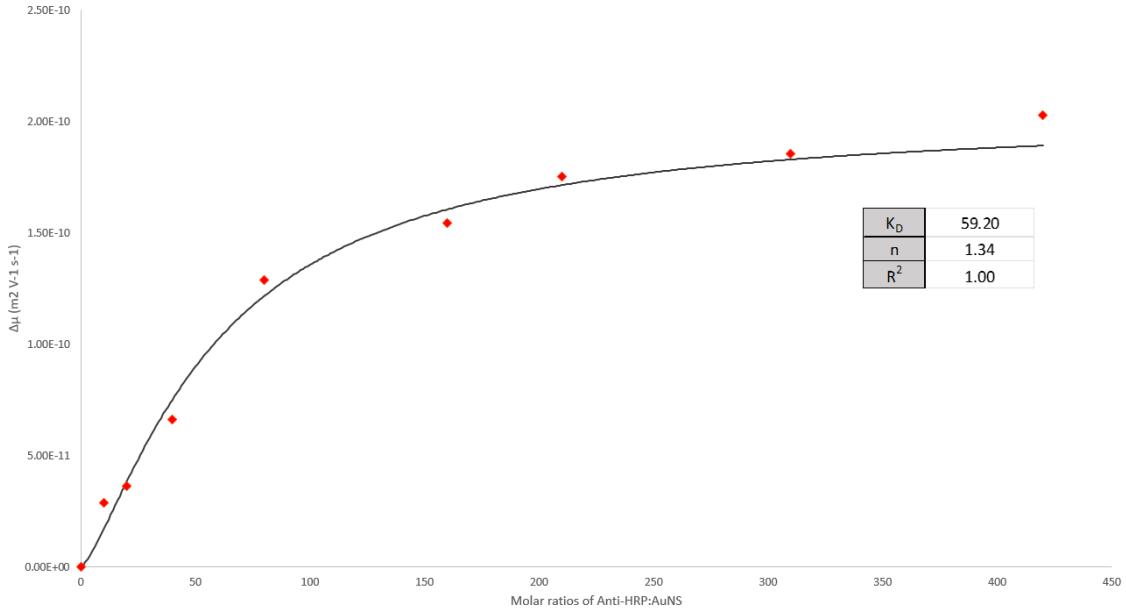

Figure 28 - Electrophoretic mobility of AuNSs with increasing concentration of anti-HRP antibody, fitted to a Hill-type adsorption isotherm. The experimental results are highlighted as red circles, and the fitting is highlighted as the black coloured sigmoidal curve. Important parameters were able to be obtained such as the K_D = 59.20, and an n =1.34.

Finally, with the BSA protein and antibody ratios studied and optimized, the full bioconjugates were assembled. To follow the formation of these bioconjugates, the process was studied by UV-Vis. As the size of the nanoparticles grows, the absorption maximum drifts shifts the LSPR of the nanoparticle to a higher wavelength since the addition of substances on the surface, namely proteins and functionalizing agents such as 11-MUA and 4-MBA, causes a change in the local refractive index, reported consistently in the literature [77], [78]. Therefore, the step-by-step formation of the AuNS bioconjugates and respective LSPR red-shifts, may be observed in figure 29.

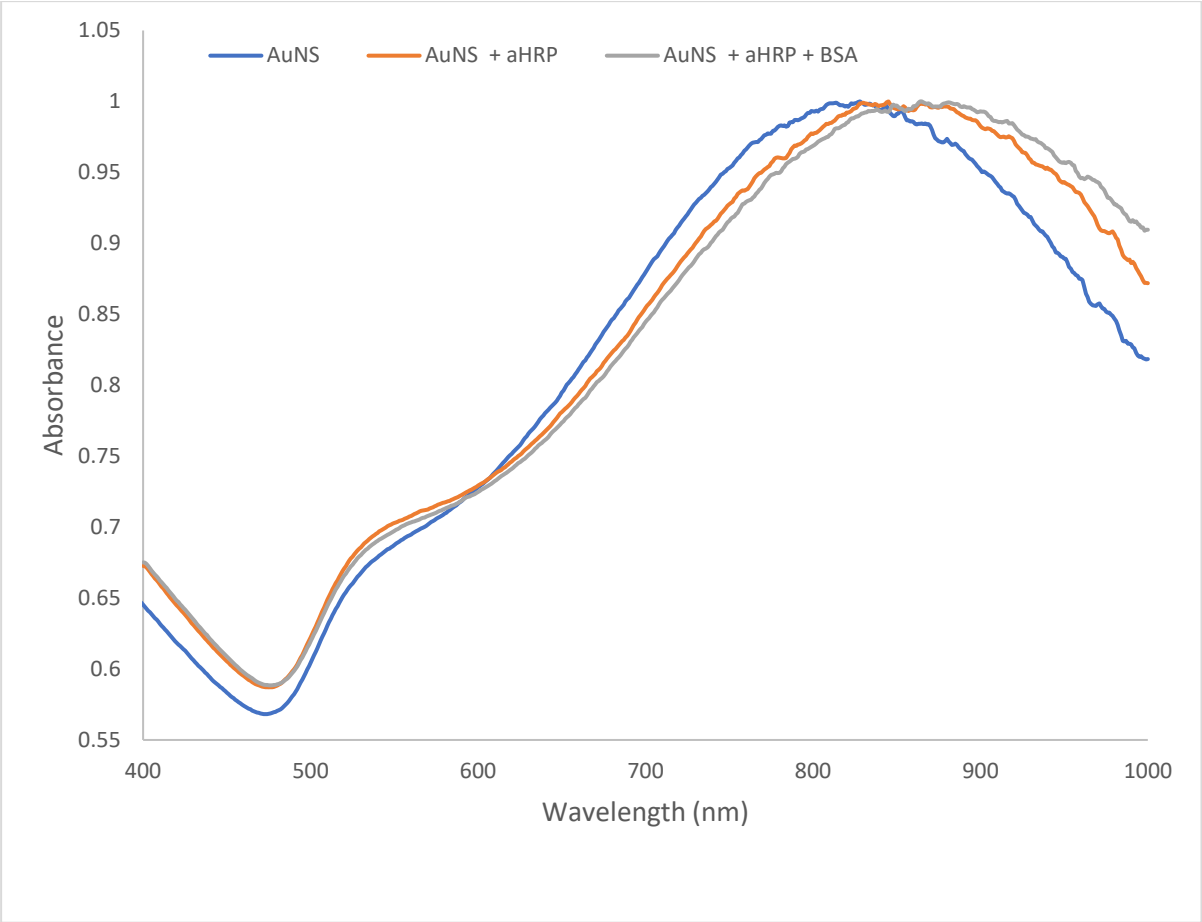

Figure 29 - Uv-Vis analysis of the conjugation process of AuNPs for the formation of bioconjugates. The figure shows a redshift of the spectra as the AuNSs radius' increases, starting with the 11-MUA and 4-MBA capped AuNSs in blue, following the conjugation with anti-HRP antibody in orange, and the full bioconjugate in green, with a very small shift. There is a broadening of the spectra as the components are added which can indicate that some aggregation is happening when proteins are added, most likely caused by crosslinking events [68].

3.1.3.3. Bioconjugate activity

During the antibody conjugation phase, the antibodies can be adsorbed in multiple conformations and not all of them may allow for the antigen to reach the binding epitopes, leading to space occupied by non-functional proteins. To assess the activity of the conjugates and to assure that these bioconjugates are capable of identifying a target antigen in a lateral flow assay, they were submitted to an enzymatic activity assay as described in section 2.5 of Material and Methods, as previously done by Tripathi K. et al [77].

AuNSs conjugates with anti-HRP antibodies and BSA were incubated with HRP at a ratio of 2100 HRP:AuNS for 1 hour, to ensure the maximum number of antibodies were filled with HRP. The samples were centrifuged and resuspended 2 times to ensure the most amount of free HRP was washed without causing full aggregation of the sample, as a 3rd centrifugation resulted in the aggregation and loss of

the AuNSs. To the measured enzymatic activities, the blank sample's activity (bioconjugate without HRP added) was subtracted (Figure 30).

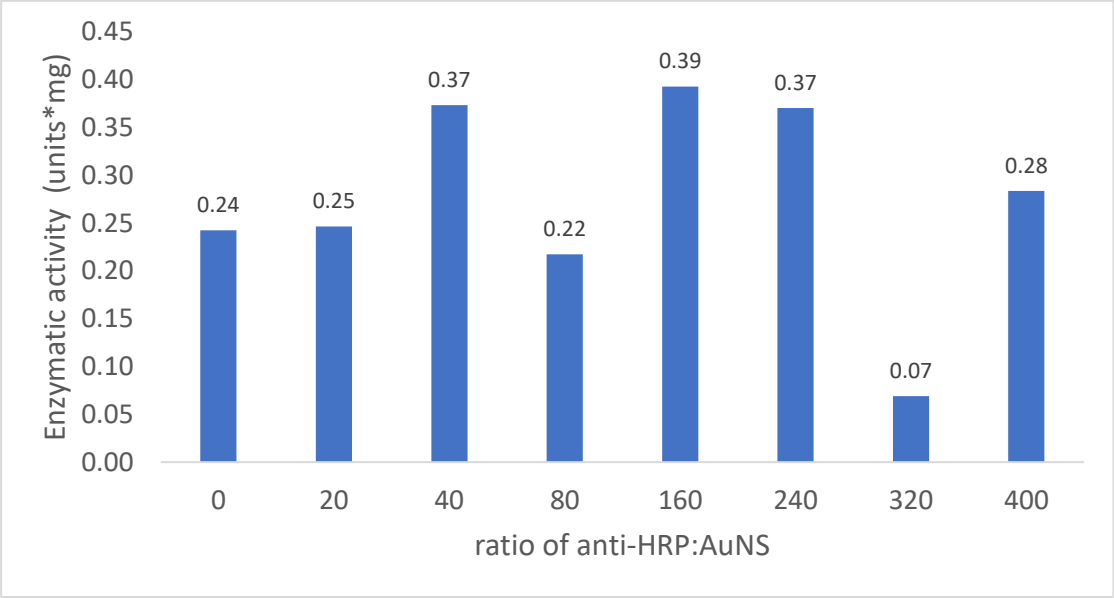

Figure 30 - Enzymatic activity of full AuNS bioconjugates. An increase in activity can be observed from a ratio of anti-HRP antibody:AuNS of 0 to 160, with an outlier at a value of 80, and a decrease in activity from 160-420. The AuNS:Anti-HRP antibody ratio can be followed at the right side of the figure

It is possible to observe, in figure 30, that there is a noteworthy amount of activity from the anti-HRP antibody:AuNS ratio of 0, which could be due to this washing process not being enough to remove most of the free HRP, however, when trying to replicate these data using only free HRP without bioconjugates, and following the same protocol and resuspension process as used with the bioconjugates, the resulting activity was equal to the blank sample, with a residual activity of 0.07 units.mg_{solid}^{-1}, 1 order of magnitude below the activity obtained for the ratio of 0 in this graph. This leads us to believe that the second hypothesis, which is the adsorption of HRP to the surface of the AuNSs, seems to be the most likely scenario. As HRP has a size of 44kDa, it may be able to adsorb onto AuNSs' surface where the blocking protein, BSA, was not able to fully cover, since this protein is bigger than HRP, with a molecular weight of 66kDa. One way to avoid this issue would be to use a smaller protein than the target protein, HRP, such as caseins. There are 5 different types of proteins, alpha-S1-casein (aS1CN), alpha-S2-casein (aS2CN), beta-casein (bCN), kappa-casein (kCN), and gamma-casein (gCN), which encompass molecular weights of 20-25kDa [82], plenty used in these types of assays [69] [70], possibly providing a better blocking effect than BSA in this case.

The maximum enzymatic activity obtained for this assay was of 0.393 units*mg^{-1}, for an Anti-HRP:AuNS ratio of 160. This value then decreases for each following increased ratio of anti-HRP antibody, until the value of 0.284 for the ratio of 420, with a decrease of 0.109 units*mg^{-1}. Compared with previous works in the same lab [75], it reports an enzymatic activity of 0.53 units*mg^{-1}, a 1.35 times higher value. This decrease can be associated to them not being conjugated using EDC/SNHS chemistry, which could lead to decreased enzymatic activity, as reported by M. J. Oliveira [76]

The same assay was performed for the AuNPs. AuNP conjugates with anti-HRP antibodies and BSA were incubated with an excess amount of HRP at a ratio of 300 HRP:AuNP, to ensure the maximum number of antibodies were filled with HRP, for 1 hour since in similar works there was no difference between an 18 hours incubation and a 1 hour incubation [77]. .The samples were centrifuged and resuspended 3 times, since these AuNP-conjugates showed increased stability in relation to the AuNS-conjugates, to

ensure the most amount of free HRP was washed, according to Tripathi et al [77]. To the measured enzymatic activities, the blank sample's activity (bioconjugate without HRP added) was subtracted (Figure 31).

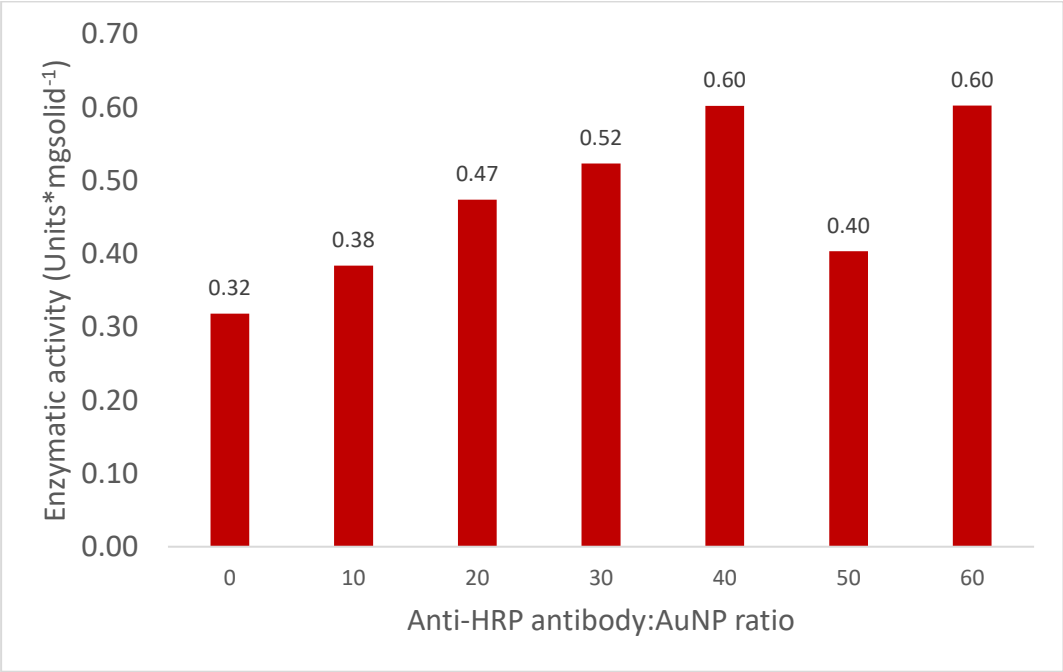

Figure 31 - Enzymatic activity of full AuNP bioconjugates. An increase in activity can be observed from a ratio of anti-HRP antibody:AuNP of 0 to 60, with a possible outlier at the value of 50. The maximum activity was reached at the ratio of 40 and the same activity value was shared by the ratio of 60.

As previously discussed in the AuNSs activity assay, we can see that the ratio of 0 anti-HRP:AuNP also shows a good amount of activity at 0.32 units*mg_{solid}^{-1}, again indicating that either the washing process was not thorough enough even with an extra washing step, or that there is still HRP adsorption to the AuNP surface even with the full blocking of the particles with BSA. With each increase in the ratio of anti-HRP antibody:AuNP, an increase in activity follows, until a maximum is achieved at a ratio of 40 and 60, with a values of 0.6 units*mg^{-1}. The value equal to the ratio of 50 shows an abrupt decrease in activity out of the line with the other values and was considered an outlier. However more assays should be performed to obtain better statistics.

3.1.3.4. SERS activity

As the AuNSs had to be functionalized also with 11-MUA, in order to guarantee good colloidal stability, this led to a lowering of the amount of 4-MBA adsorbed onto the AuNSs surfaces. However, as seen in figure 32, the associated Raman peaks for 4-MBA were still very well defined, showing that the number of 4-MBA molecules adsorbed onto the surface was still enough for SERS detection. Another point of worry would be the very intense vibrational lines associated to nitrocellulose interfering with those of 4-MBA, however, as also shown in figure 32, vibrational lines 1 (1079 cm^{-1}) and 2 (1587 cm^{-1}), corresponding to the aromatic ring vibrations [85], show different positions from the main vibrational lines of nitrocellulose at 846 cm^{-1}, 1286 cm^{-1}. There is a small superposition of the 1122 cm^{-1} with line 1 of 4-MBA, but no superpositions are observed with line 2. Therefore, SERS vibrational line 2 (1587 cm^{-1}) of 4-MBA, was chosen as reference for the LFA assays.

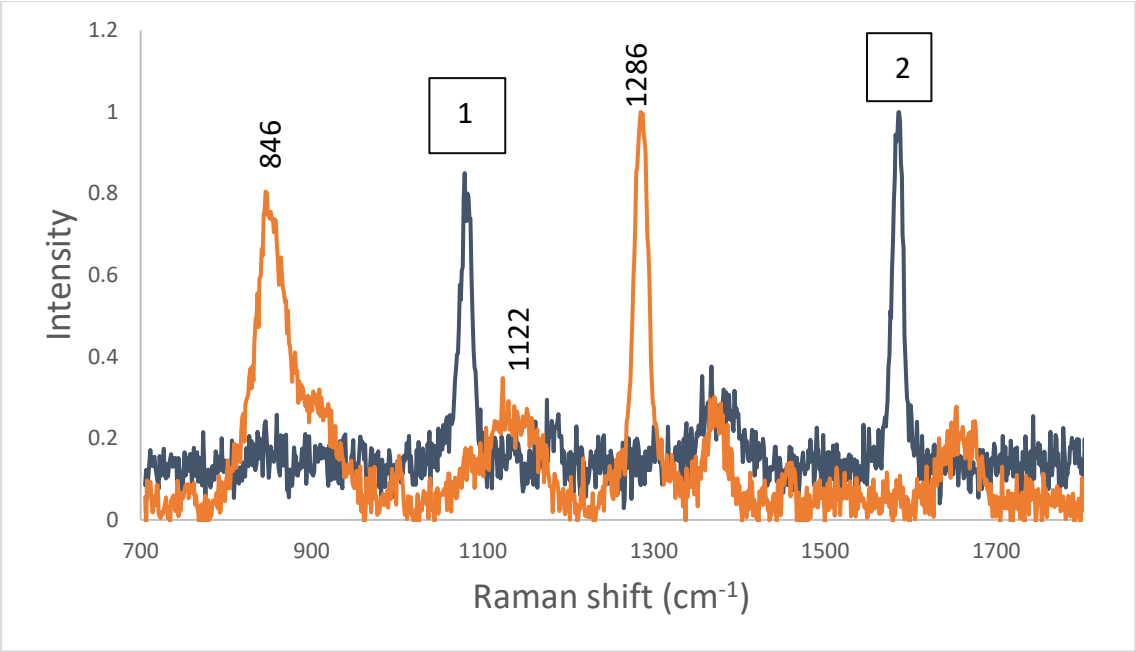

Figure 32 - Normalized intensity of the Raman spectrum of nitrocellulose (orange) and the SERS spectrum of 4-MBA and 11-MUA functionalized AuNSs (dark blue). The main lines associated with 4-MBA are marked with the numbers 1 – 1079 cm^{-1} line, and 2 - 1587 cm^{-1} line.

3.2. Lateral Flow assay

With the SERS tags optimised, a shift from anti-HRP antibody to anti-GFAP was attempted for use in the LFA, however this would result in the aggregation of the nanostars during the conjugation phase, leading us to change to using anti-HRP due to time constrictions.

For the final process of creating a highly sensitive LFA proof of concept, the SERS tags composed of AuNSs conjugated with antibodies and BSA, were used as markers for identification of the target antigen in the sample. This assay has the capability of being both qualitative, by identifying with colour a positive or negative test, and quantitative, by using the help of a Raman measuring device coupled with the Raman tag 4-MBA, allowing a fast and/or accurate measure.

The LFA test was designed to be non-competitive as it final objective is to identify the existence of GFAP in blood, based on the formation of a "sandwich" with nitrocellulose adsorbed antibodies, the target antigen, and the SERS tags for a visual and quantifiable signal (figure 33).

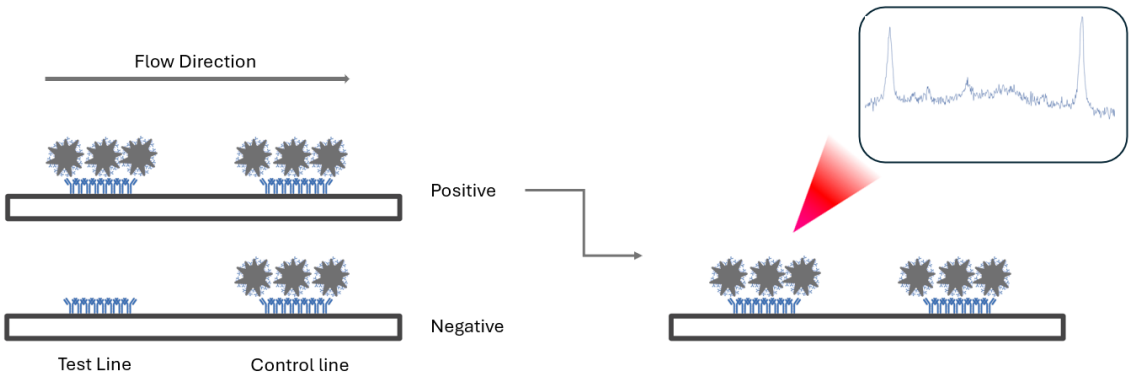

Figure 33 – Schematic of the LFA and data attainment for the diagnosis of the relevant antigen, in this case, GFAP.

3.2.1. Nitrocellulose membrane selection

The LFA kit has several types of nitrocellulose membranes with different characteristics: the degree of protein binding, varying from CNPF - low protein binding – to CNPC – higher protein binding – and finally to CNPH with the highest protein binding. Another varying parameter is pore size, which dictates how slow a sample should flow through the membrane, translated in wicking times of (70 ± 12) s, (90 ± 15) s, (150 ± 20) s and (200 ± 35) s [86]. Due to time constraints and according to the work of Tomás et al [83] using the same commercial kit, the highest binding type of membrane, CPNH, was chosen for further tests.
Using the CNPH type membrane, an assay for each of the pore sizes was made by using 10 µL of a PBS and BSA mixture, henceforth called PBS-B, at PBS 2x and BSA at 2mg/mL, 10 µL of the running sample at 0.2 nM and 5 µL of tween-20 at 10%. Results are shown in figure 34.

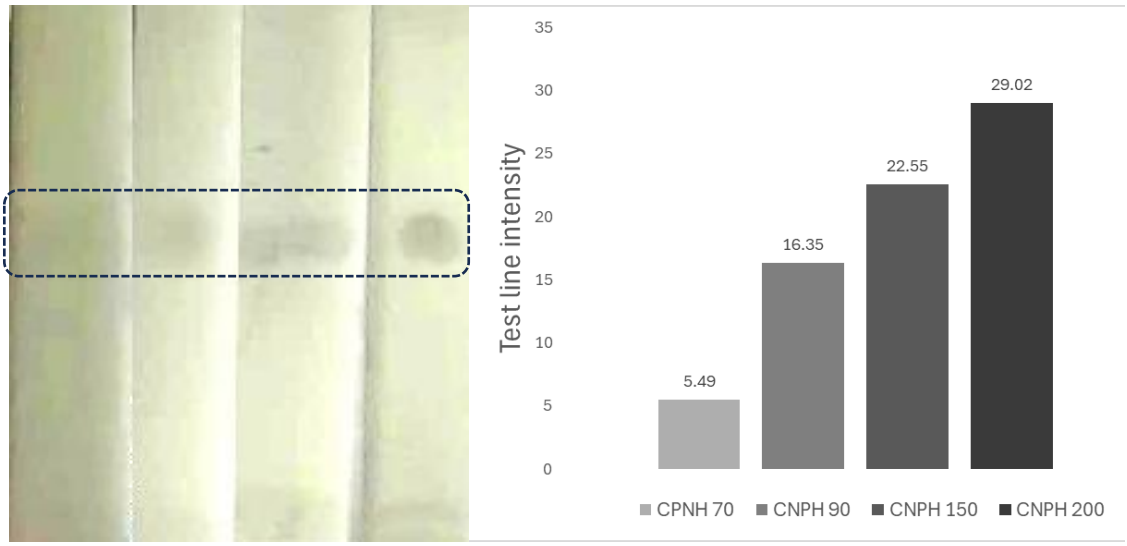

Figure 34 – Nitrocellulose membrane selection process. The LFAs are displayed on the left and, on the right, the average pixel intensity difference between the test line and the background.

From the results obtained in figure 34, we concluded that the best nitrocellulose membrane would be the CPNH 200 due to obtaining the highest average pixel intensity. As expected, the average pixel intensity increases as the pore size increases, from 70 to 200, as SERS tags take longer to run through the membrane, allowing more time for conjugation with the immobilized antibodies on the test line. In further optimization procedures, the CNPH 150 nitrocellulose membrane was chosen instead of the 200 CNPH version due to the latter having ran out. Curiously enough, no control line was found in any of the LFAs, leading us to believe that most of the SERS tags used bound to the test line. As the signal was quite faded, even in the higher pore size membranes, the concentration of SERS tags used was increased to 1 nM.

3.2.2. Sensitivity tests

Focusing on determining the limit of detection, several LFAs were ran with the same conditions as in section 3.2.1., changing the SERS tags concentration to 1 nM and varying the concentration of HRP between 1.8 mg and 1.8mg, as seen in figures 35 and 36.

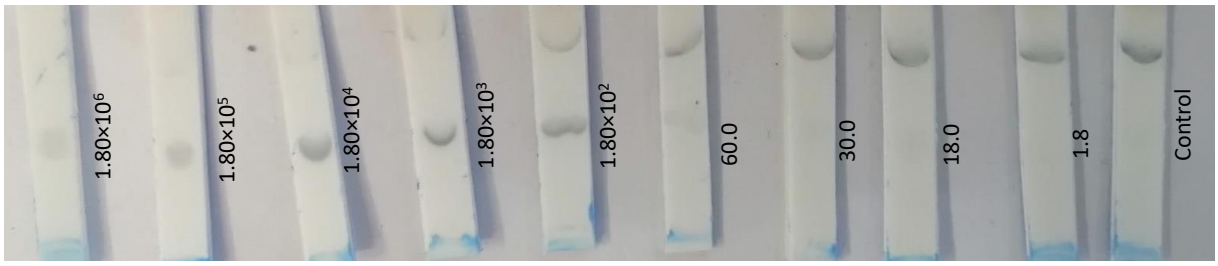

Figure 35 - LFAs for sensitivity assessment, expressed in milligrams. The concentration was serially diluted starting at 1.8 mg, on the left, to 1.8 ng to the second to last on the right. The rightmost LFA represent the control sample with 0 HRP concentration.

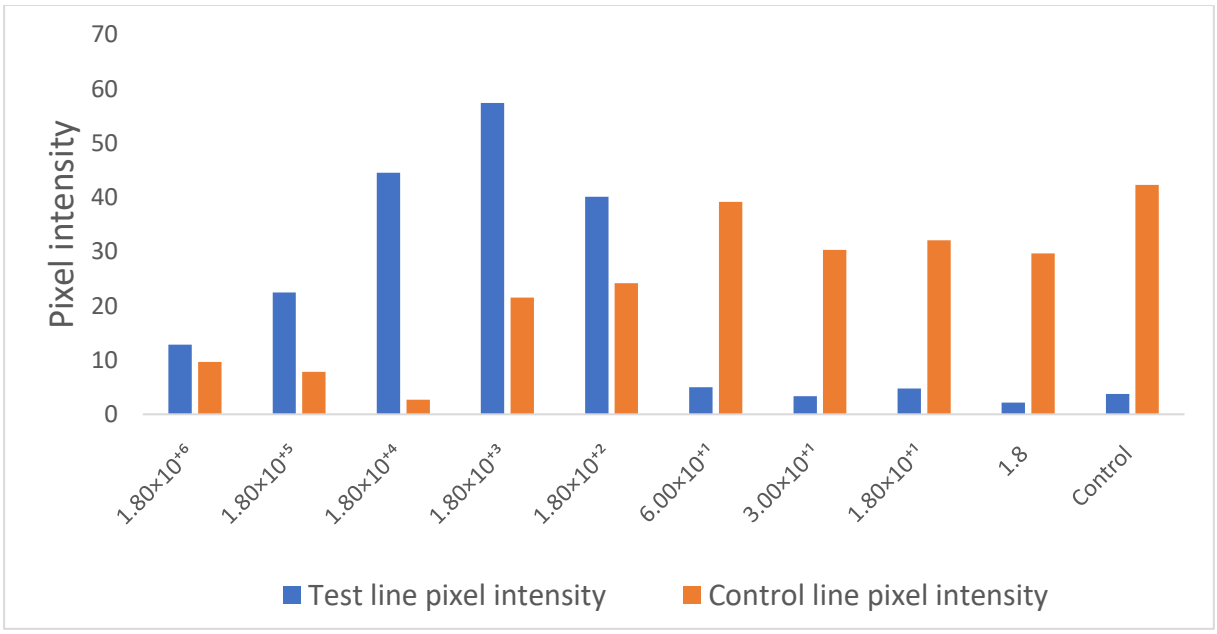

Figure 36 - Change in pixel intensity of test line and control line over the decrease in HRP concentration in nanograms. Concentration was serially diluted starting at 1.8 mg on the left, to 1.8 ng. The rightmost bars represent the control LFA, with a concentration of HRP of 0.

By looking at the data shown in in figure 36, a trend seems to appear with the increase of the test line intensity on the tests with concentrations between 1.8mg and 180ng. The test line intensity starts low, probably due to the high excess of antigen sample fully covering both the antibody epitopes present in the SERS tags and on the test line, decreasing the probably of a sandwich being formed there. Both the test line and the control line either did not appear or were very faded on the higher concentration assays (1.8mg to 18 µg) however, as the concentration of the antigen decreases, there appears to be an increase in intensity of the control line from the 1.8 µg HRP to 1.8 ng concentration, signifying a growing amount of non-bound SERS tags to the test line that bind to the control line. The limit of visual readout was determined to be between 180 ng/mL and 60ng/mL, with more assays needing to be done to acquire a more detailed value.

3.2.3. SERS measurements

In view of the creation of a preliminary prototype of the LFA, the SERS signal was measured for the nitrocellulose membranes established in section 3.2.1. the objective of these measurements was to assess which membrane concentrates the sample the most and consequently produces the most intense signal, necessary to achieve a highly sensitive assay. Various measures were taken on different locations of the test line and the results are displayed in figure 37, with the average integral value of each band calculated between 1560 and 1600 cm^{-1}, together with the standard deviation.

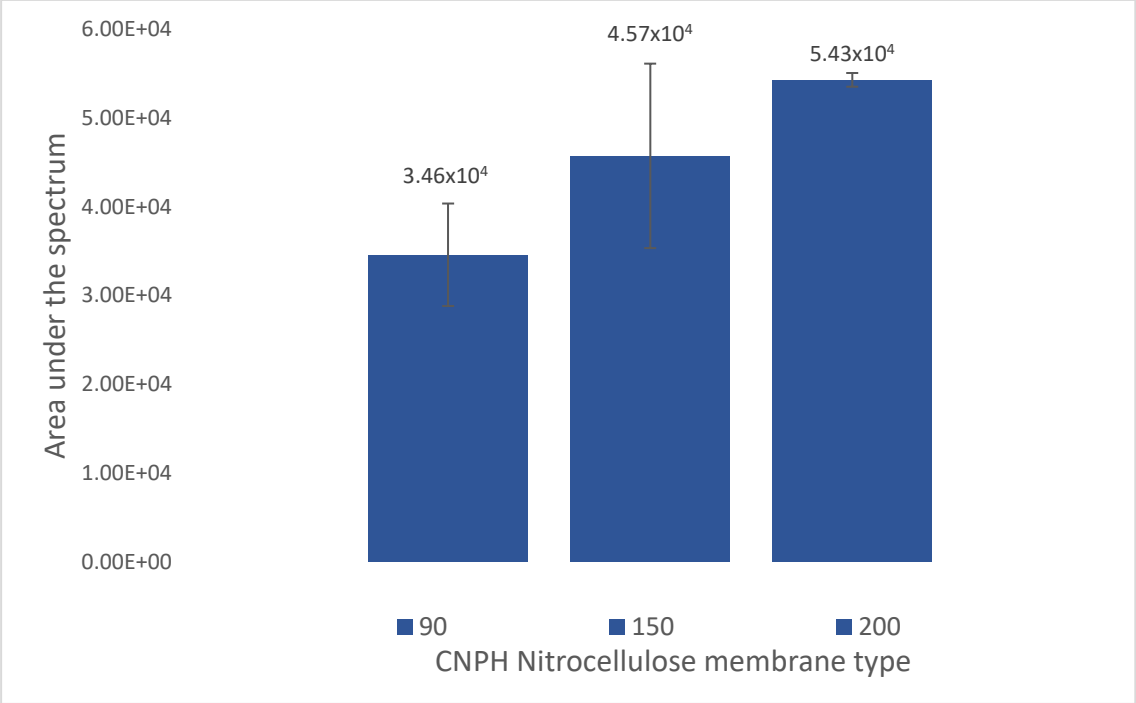

Figure 37- Nitrocellulose membrane types and respective SERS signal. SERS signal was measured using its integrated area (a.u.cm^{-1}) under the spectrum, with a baseline between 1560 and 1600 cm^{-1}.

As previously mentioned, the difference between pixel intensity between CNPH 200 and CNPH 150 was favoured towards the former, however, these two showed close results in terms of signal intensity, showing that CNPH 150 is a good choice for a nitrocellulose membrane although with high variability which could be due to the deposition method.

Next, SERS measurements were taken of the various concentrations, and the area under the spectrum between 1560 and 1600 cm^{-1} was calculated. Different measurements were taken in different locations of the test line and the average was calculated, as well as the standard deviation. They were obtained as such, in figure 37.

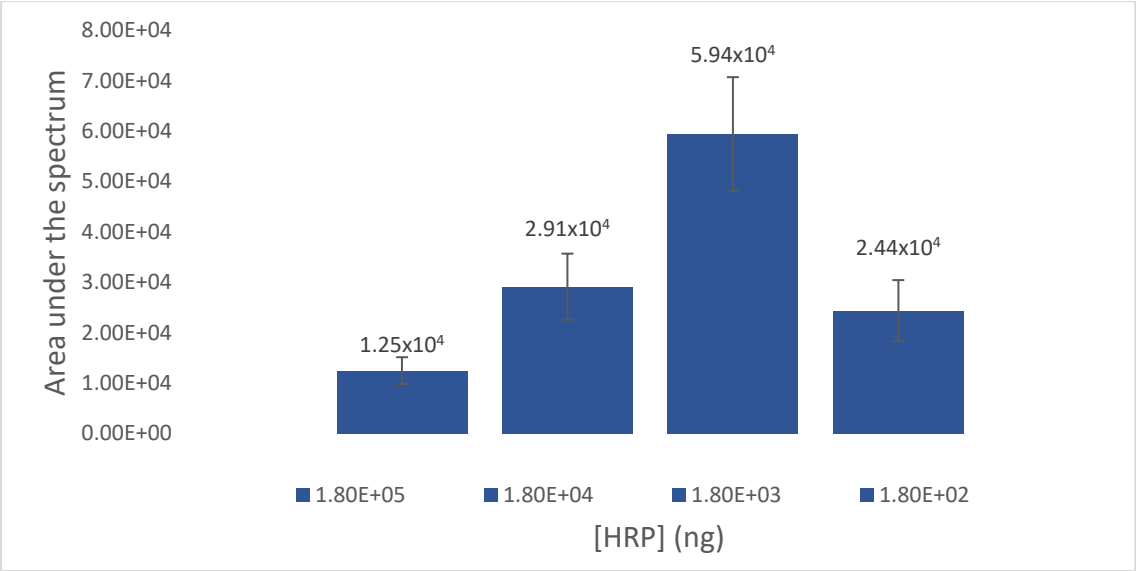

Figure 38 – Integrated area under the spectrum (a.u.cm$^{-1)}$ of the SERS measurements performed on LFA tests, with concentrations equal to those shown in figure 36.

As shown above and comparing to figure 36 which shows the increase in intensity of the lines in each LFA, we can see that there is a correlation between the intensity of the test line and the measured SERS value. As the intensity increases from $1.8x10^5$ ng of peroxidase to $1.8x10^3$ ng, an increase in SERS activity follows, from $1.25x10^4 \pm 2.66x10^3$ to $5.94x10^4 \pm 1.13x10^4$ a.u.cm^{-1}. And then, just as the intensity starts decreasing as the concentration of antigen decreases, so does the SERS intensity of the corresponding LFA. After this concentration, none of the other test lines were visible or detectable with SERS, reinforcing that the limit of detection is between 180 ng and 60 ng of peroxidase.

This assay shows the potential of SERS testing as an ultrasensitive tool for the quantification of the target antigen on the test line, as previous authors have already shown for the detection of other antigens [87]. This experiment shows the limits of SERS as a tool for detecting this antigen, as the loss of visibility corresponds to a loss of signal, however, this could be due to the way that the test line is prepared, which is by hand, that can lead the antibodies to not be evenly spread out, resulting in the SERS tags concentrating on a point which was not “caught” by the SERS analysis.

3.3. Conclusion

A working dipstick LFA was able to be developed using AuNSs for qualitative and quantitative assessment, using SERS and the SERS tag 4-MBA for signal quantification, utilizing anti-HRP antibody as a model for further development into a GFAP diagnosis tool. Promising results for use of AuNPs as a simpler qualitative diagnosis tool were also obtained.

AuNPs were able to be synthetised, with the characterization showing a good polydispersity (< 0.3) and size of 12nm. The concentrations of anti-HRP and BSA were obtained and optimised for both AuNSs and AuNPs, with the AuNPs requiring an extra treatment with EDC/SNHS to further increase the conjugation efficiency. AuNSs stability was improved by changing the functionalization agent from 4-MBA to a 1:1 mixture of 4-MBA and 11-MUA, making use of the widely studied and used 11-MUA to decrease aggregation without losing the ultrasensitive aspect of the 4-MBA nanostars. These conjugates were able to be characterised by techniques such as DLS, Uv-Vis, AGE and enzymatic activity assays, essential for following the bioconjugate formation and ensure that every procedure is going as expected. DLS showed the formation of the full bioconjugate of the AuNPs by calculating the increase in R_H, signifying the adherence of proteins (antibody, BSA, peroxidase) on its surface either by self-assembled monolayers, or antibody epitope interaction. Uv-Vis showed the change in refractive index following the conjugation of each nanoparticle with proteins, showing an increase towards higher wavelengths as expected. AGE was used to optimise the concentration of protein necessary for a full nanoparticle coating, necessary for maximum analyte detection. Enzymatic activity assays were performed and managed to further assess the optimal concentration of antibody needed for maximum detection, showing that, on the AuNSs used, a ratio of 160 anti-HRP antibody:AuNSs is preferable than the maximum coating of 420 obtained by AGE. As the conjugates were shifted from the model antibody anti-HRP to the anti-GFAP, necessary for detecting GFAP, difficulties occurred where the optimal amount of anti-GFAP, as assessed by, anti-HRO, would result in aggregation. This resulted in the use of anti-HRP for the LFAs to obtain a proof-of-concept and optimise more parameters.

LFA conditions were optimised for running a sample of AuNSs bioconjugates, with the conditions of 2mM KPB at pH 7.4 mixed with 1x PBS and 1mg/mL BSA resulting in a run with minimal non-specific interactions, an ever-present problem in LFA development. The most appropriate LFA nitrocellulose membrane was chosen by both SERS signal and pixel intensity, with the result being the choice of CNPH 150, with higher SERS signal but slightly lower pixel intensity. Finally, sensitivity assays were run on LFAs, with decreasing concentration of HRP, from 1.8mg until 1.8ng, with the cutoff value for visual assessment being of between 180ng and 60ng, and a SERS signal cutoff value in the same amount.

3.4. Future perspectives

For obtaining a lower limit of detection and being able to detect TBI and mTBI, the AuNSs and LFAs need further optimization. AuNSs are inherently not as stable as their round counterparts, and this difference is very noticeable during the characterization and conjugation phases. The washing steps would almost always result in aggregation of AuNSs even at low rcfs, such as 1200, leading to a necessity in either increasing their stability during the synthesis stage, like the addition of 11-MUA as a functionalization agent, or the use of dialysis since this would allow for the washing of the solution without exerting high forces onto the AuNSs, causing aggregation, in exchange of higher washing times with each washing step.

Further optimisation for the LFA is also necessary, as for higher concentrations of peroxidase there seemed to be a decrease in signal on the test line, and a smoother progression through the dilutions since from the 180ng to 60ng, there was an almost complete loss of test line signal.

After this proof-of-concept using anti-peroxidase antibody and peroxidase as the antigen, a transition with the use of anti-GFAP for targeting the GFAP biomarker should be made to develop the actual SERS tags used to detect TBI. This involves the re-optimization of the AuNS incubation with anti-GFAP antibodies as during this work, it was noticed that incubation of AuNSs with the optimised quantity of anti-GFAP resulted in aggregation.

SERS activity measurements need further work replicates, as these were measured using only one LFA strip each, with triplicate measures in different locations of the lines. Maps need to be done to be able to assess the differences between SERS signal intensity over various spots, with the 20% laser intensity or higher for LFAs with very weakly visible test lines.

Finally, the test and control line preparation method influence the distribution of antibodies. By manually pipetting the solution, a coffee ring effect is induced which causes a high concentration of antibodies to be deposited on the edge of the drop. This method causes a very large variability between test and control lines across replicates, causing difficulties when analysing these for Limit of Detection (LoD) and Limit of Quantification (LoQ) assessment, or just general optimisation procedures as the pixel intensity difference between 2 close dilutions may be caused by this “random” distribution of antibodies on the nitrocellulose strip. This issue could be solved by using a strip deposition equipment, as are normally used in industrial conditions, which would deposit the antibodies homogeneously among the strips.With enough optimisation and time, by implementing these changes and considerations, especially by acquiring an automatic line dispenser, an ultrasensitive LFA based on SERS detection could take shape, leading to innovation on the TBI diagnosis market.

References

[1] M. C. Dewan *et al.*, 'Estimating the global incidence of traumatic brain injury', *J Neurosurg*, vol. 130, no. 4, pp. 1080–1097, Apr. 2018, doi: 10.3171/2017.10.JNS17352.

[2] 'SURVEILLANCE REPORT', 2018.

[3] GBD 2016 Traumatic Brain Injury and Spinal Cord Injury Collaborators, 'Global, regional, and national burden of traumatic brain injury and spinal cord injury, 1990-2016: a systematic analysis for the Global Burden of Disease Study 2016', *Lancet Neurol*, vol. 18, no. 1, pp. 56–87, Jan. 2019, doi: 10.1016/S1474-4422(18)30415-0.

[4] 'TBI Data | Concussion | Traumatic Brain Injury | CDC Injury Center'. Accessed: Oct. 02, 2023. [Online]. Available: https://www.cdc.gov/traumaticbraininjury/data/index.html

[5] H. M. Bramlett and W. D. Dietrich, 'Long-Term Consequences of Traumatic Brain Injury: Current Status of Potential Mechanisms of Injury and Neurological Outcomes', *J Neurotrauma*, vol. 32, no. 23, pp. 1834–1848, Dec. 2015, doi: 10.1089/neu.2014.3352.

[6] K. Pierre, K. Dyson, A. Dagra, E. Williams, K. Porche, and B. Lucke-Wold, 'Chronic Traumatic Encephalopathy: Update on Current Clinical Diagnosis and Management', *Biomedicines*, vol. 9, no. 4, p. 415, Apr. 2021, doi: 10.3390/biomedicines9040415.

[7] 'Traumatic Brain Injury (TBI)', National Institute of Neurological Disorders and Stroke. Accessed: Oct. 03, 2023. [Online]. Available: https://www.ninds.nih.gov/health-information/disorders/traumatic-brain-injury-tbi

[8] 'Traumatic brain injury-Traumatic brain injury - Symptoms & causes', Mayo Clinic. Accessed: Oct. 03, 2023. [Online]. Available: https://www.mayoclinic.org/diseases-conditions/traumatic-brain-injury/symptoms-causes/syc-20378557

[9] 'Traumatic brain injury-Traumatic brain injury - Diagnosis & treatment', Mayo Clinic. Accessed: Oct. 09, 2023. [Online]. Available: https://www.mayoclinic.org/diseases-conditions/traumatic-brain-injury/diagnosis-treatment/drc-20378561

[10] 'CT scan - Mayo Clinic'. Accessed: Oct. 09, 2023. [Online]. Available: https://www.mayoclinic.org/tests-procedures/ct-scan/about/pac-20393675

[11] 'MRI - Mayo Clinic'. Accessed: Oct. 09, 2023. [Online]. Available: https://www.mayoclinic.org/tests-procedures/mri/about/pac-20384768

[12] J. Žurek, 'Biomarkers in Traumatic Brain Injury', in *Essentials of Neuroanesthesia*, Elsevier, 2017, pp. 587–591. doi: 10.1016/B978-0-12-805299-0.00033-6.

[13] A. Dadas, J. Washington, R. Diaz-Arrastia, and D. Janigro, 'Biomarkers in traumatic brain injury (TBI): a review', *Neuropsychiatr Dis Treat*, vol. 14, pp. 2989–3000, Nov. 2018, doi: 10.2147/NDT.S125620.

[14] J. J. S. Rickard, V. Di-Pietro, D. J. Smith, D. J. Davies, A. Belli, and P. G. Oppenheimer, 'Rapid optofluidic detection of biomarkers for traumatic brain injury via surface-enhanced Raman spectroscopy', *Nat Biomed Eng*, vol. 4, no. 6, pp. 610–623, Feb. 2020, doi: 10.1038/s41551-019-0510-4.

[15] K. Strimbu and J. A. Tavel, 'What are Biomarkers?', *Curr Opin HIV AIDS*, vol. 5, no. 6, pp. 463–466, Nov. 2010, doi: 10.1097/COH.0b013e32833ed177.

[16] T. Abboud, V. Rohde, and D. Mielke, 'Mini review: Current status and perspective of S100B protein as a biomarker in daily clinical practice for diagnosis and prognosticating of clinical outcome in patients with neurological diseases with focus on acute brain injury', *BMC Neuroscience*, vol. 24, no. 1, p. 38, Jul. 2023, doi: 10.1186/s12868-023-00807-2.

[17] I. Hossain, N. Marklund, E. Czeiter, P. Hutchinson, and A. Buki, 'Blood biomarkers for traumatic brain injury: A narrative review of current evidence', *Brain and Spine*, vol. 4, p. 102735, Jan. 2024, doi: 10.1016/j.bas.2023.102735.

[18] I. Hossain *et al.*, 'Admission Levels of Total Tau and β-Amyloid Isoforms 1–40 and 1–42 in Predicting the Outcome of Mild Traumatic Brain Injury', *Front. Neurol.*, vol. 11, May 2020, doi: 10.3389/fneur.2020.00325.

[19] A. Abdelhak *et al.*, 'Blood GFAP as an emerging biomarker in brain and spinal cord disorders', *Nat Rev Neurol*, vol. 18, no. 3, Art. no. 3, Mar. 2022, doi: 10.1038/s41582-021-00616-3.

[20] Z. Yang and K. K. W. Wang, 'Glial Fibrillary acidic protein: From intermediate filament assembly and gliosis to neurobiomarker', *Trends Neurosci*, vol. 38, no. 6, pp. 364–374, Jun. 2015, doi: 10.1016/j.tins.2015.04.003.

[21] J. J. Bazarian *et al.*, 'Serum GFAP and UCH-L1 for prediction of absence of intracranial injuries on head CT (ALERT-TBI): a multicentre observational study', *The Lancet Neurology*, vol. 17, no. 9, pp. 782–789, Sep. 2018, doi: 10.1016/S1474-4422(18)30231-X.

[22] M. Y. Mahan *et al.*, 'Glial Fibrillary Acidic Protein (GFAP) Outperforms S100 Calcium-Binding Protein B (S100B) and Ubiquitin C-Terminal Hydrolase L1 (UCH-L1) as Predictor for Positive Computed Tomography of the Head in Trauma Subjects', *World Neurosurgery*, vol. 128, pp. e434–e444, Aug. 2019, doi: 10.1016/j.wneu.2019.04.170.

[23] N. A. Huebschmann *et al.*, 'Comparing Glial Fibrillary Acidic Protein (GFAP) in Serum and Plasma Following Mild Traumatic Brain Injury in Older Adults', *Front. Neurol.*, vol. 11, Sep. 2020, doi: 10.3389/fneur.2020.01054.

[24] M. Brenner and A. Messing, 'Regulation of GFAP Expression', *ASN Neuro*, vol. 13, p. 1759091420981206, Feb. 2021, doi: 10.1177/1759091420981206.

[25] K. M. Koczula and A. Gallotta, 'Lateral flow assays', *Essays in Biochemistry*, vol. 60, no. 1, p. 111, Jun. 2016, doi: 10.1042/EBC20150012.

[26] 'Lateral Flow Assays Market Size And Share Report, 2030'. Accessed: Jun. 30, 2024. [Online]. Available: https://www.grandviewresearch.com/industry-analysis/lateral-flow-assay-market

[27] E. B. Bahadır and M. K. Sezgintürk, 'Lateral flow assays: Principles, designs and labels', *TrAC Trends in Analytical Chemistry*, vol. 82, pp. 286–306, Sep. 2016, doi: 10.1016/j.trac.2016.06.006.

[28] 'Traumatic Brain Injuries Assessment Market Size Report, 2032', Global Market Insights Inc. Accessed: Oct. 03, 2024. [Online]. Available: https://www.gminsights.com/industry-analysis/traumatic-brain-injuries-assessment-market

[29] 'i-STAT TBI Cartridge'. Accessed: Oct. 03, 2024. [Online]. Available: https://www.globalpointofcare.abbott/us/en/product-details/apoc/istat-tbi.html

[30] O. of the Commissioner, 'FDA authorizes marketing of first blood test to aid in the evaluation of concussion in adults', FDA. Accessed: Oct. 03, 2024. [Online]. Available: https://www.fda.gov/news-events/press-announcements/fda-authorizes-marketing-first-blood-test-aid-evaluation-concussion-adults

[31] 'VIDAS® TBI (GFAP, UCH-L1)', bioMérieux Website. Accessed: Oct. 03, 2024. [Online]. Available: https://www.biomerieux.com/corp/en/our-offer/clinical-products/vidas-tbi-gfap-uch-l1.html

[32] P. Howitt *et al.*, 'Technologies for global health', *The Lancet*, vol. 380, no. 9840, pp. 507–535, Aug. 2012, doi: 10.1016/S0140-6736(12)61127-1.

[33] '5: Raman Spectroscopy', Chemistry LibreTexts. Accessed: Jul. 09, 2024. [Online]. Available: https://chem.libretexts.org/Bookshelves/Analytical_Chemistry/Molecular_and_Atomic_Spectroscopy_(Wenzel)/5%3A_Raman_Spectroscopy

[34] X. Wang, S.-C. Huang, S. Hu, S. Yan, and B. Ren, 'Fundamental understanding and applications of plasmon-enhanced Raman spectroscopy', *Nat Rev Phys*, vol. 2, no. 5, pp. 253–271, Apr. 2020, doi: 10.1038/s42254-020-0171-y.

[35] 'Nanotechnology Timeline | National Nanotechnology Initiative'. Accessed: Jul. 04, 2024. [Online]. Available: https://www.nano.gov/timeline

[36] N. Joudeh and D. Linke, 'Nanoparticle classification, physicochemical properties, characterization, and applications: a comprehensive review for biologists', *Journal of Nanobiotechnology*, vol. 20, no. 1, p. 262, Jun. 2022, doi: 10.1186/s12951-022-01477-8.

[37] J. Turkevich, P. C. Stevenson, and J. Hillier, 'A study of the nucleation and growth processes in the synthesis of colloidal gold', *Discuss. Faraday Soc.*, vol. 11, p. 55, 1951, doi: 10.1039/df9511100055.

[38] I. Ojea-Jiménez, N. G. Bastús, and V. Puntes, 'Influence of the Sequence of the Reagents Addition in the Citrate-Mediated Synthesis of Gold Nanoparticles', *J. Phys. Chem. C*, vol. 115, no. 32, pp. 15752–15757, Aug. 2011, doi: 10.1021/jp2017242.

[39] S. Shrestha, B. Wang, and P. Dutta, 'Nanoparticle processing: Understanding and controlling aggregation', *Advances in Colloid and Interface Science*, vol. 279, p. 102162, May 2020, doi: 10.1016/j.cis.2020.102162.

[40] H. Lee, 'Hydrodynamics and Aggregation of Nanoparticles with Protein Corona: Effects of Protein Concentration and Ionic Strength', *Small*, vol. n/a, no. n/a, p. 2403913, doi: 10.1002/smll.202403913.

[41] S. J. Amina and B. Guo, 'A Review on the Synthesis and Functionalization of Gold Nanoparticles as a Drug Delivery Vehicle', *Int J Nanomedicine*, vol. 15, pp. 9823–9857, Dec. 2020, doi: 10.2147/IJN.S279094.

[42] M. H. Jazayeri, H. Amani, A. A. Pourfatollah, H. Pazoki-Toroudi, and B. Sedighimoghaddam, 'Various methods of gold nanoparticles (GNPs) conjugation to antibodies', *Sensing and Bio-Sensing Research*, vol. 9, pp. 17–22, Jul. 2016, doi: 10.1016/j.sbsr.2016.04.002.

[43] K. M. Kosuda, J. M. Bingham, K. L. Wustholz, R. P. Van Duyne, and R. J. Groarke, 'Nanostructures and Surface-Enhanced Raman Spectroscopy', in *Comprehensive Nanoscience and Nanotechnology*, Elsevier, 2016, pp. 117–152. doi: 10.1016/B978-0-12-803581-8.00611-1.

[44] V. Amendola, R. Pilot, M. Frasconi, O. M. Maragò, and M. A. Iatì, 'Surface plasmon resonance in gold nanoparticles: a review', *J. Phys.: Condens. Matter*, vol. 29, no. 20, p. 203002, May 2017, doi: 10.1088/1361-648X/aa60f3.

[45] B. Sharma, R. R. Frontiera, A.-I. Henry, E. Ringe, and R. P. Van Duyne, 'SERS: Materials, applications, and the future', *Materials Today*, vol. 15, no. 1, pp. 16–25, Jan. 2012, doi: 10.1016/S1369-7021(12)70017-2.

[46] X. Han and B. Zhao, 'Surface-enhanced Raman scattering (SERS) and applications', in *Molecular and Laser Spectroscopy*, Elsevier, 2020, pp. 349–386. doi: 10.1016/B978-0-12-818870-5.00010-1.

[47] C. Lin *et al.*, 'Recent development of surface-enhanced Raman scattering for biosensing', *Journal of Nanobiotechnology*, vol. 21, no. 1, p. 149, May 2023, doi: 10.1186/s12951-023-01890-7.

[48] I. B. Becerril-Castro *et al.*, 'Gold Nanostars: Synthesis, Optical and SERS Analytical Properties', *Analysis & Sensing*, vol. 2, no. 3, p. e202200005, 2022, doi: 10.1002/anse.202200005.

[49] X. Fu, Z. Cheng, J. Yu, P. Choo, L. Chen, and J. Choo, 'A SERS-based lateral flow assay biosensor for highly sensitive detection of HIV-1 DNA', *Biosensors and Bioelectronics*, vol. 78, pp. 530–537, Apr. 2016, doi: 10.1016/j.bios.2015.11.099.

[50] X. Liu *et al.*, 'A nanogap-enhanced SERS nanotag–based lateral flow assay for ultrasensitive and simultaneous monitoring of SARS-CoV-2 S and NP antigens', *Microchim Acta*, vol. 191, no. 2, p. 104, Jan. 2024, doi: 10.1007/s00604-023-06126-x.

[51] A. Georges and J. M. Das, 'Traumatic Brain Injury (Archive)', in *StatPearls*, Treasure Island (FL): StatPearls Publishing, 2024. Accessed: Jul. 14, 2024. [Online]. Available: http://www.ncbi.nlm.nih.gov/books/NBK459300/

[52] D. O. Okonkwo *et al.*, 'Brain Tissue Oxygen Monitoring and Management in Severe Traumatic Brain Injury (BOOST-II): a Phase II Randomized Trial', *Crit Care Med*, vol. 45, no. 11, pp. 1907–1914, Nov. 2017, doi: 10.1097/CCM.0000000000002619.

[53] W. Lin, R.-W. Zhang, S.-S. Jang, C.-P. Wong, and J.-I. Hong, '"Organic Aqua Regia"—Powerful Liquids for Dissolving Noble Metals', *Angewandte Chemie International Edition*, vol. 49, no. 43, pp. 7929–7932, 2010, doi: 10.1002/anie.201001244.

[54] P. K. Smith *et al.*, 'Measurement of protein using bicinchoninic acid', *Analytical Biochemistry*, vol. 150, no. 1, pp. 76–85, Oct. 1985, doi: 10.1016/0003-2697(85)90442-7.

[55] M. Bento, 'Nanopartículas plasmónicas para biodeteção por Raman'. 2019.

[56] W. Haiss, N. T. K. Thanh, J. Aveyard, and D. G. Fernig, 'Determination of Size and Concentration of Gold Nanoparticles from UV−Vis Spectra', *Anal. Chem.*, vol. 79, no. 11, pp. 4215–4221, Jun. 2007, doi: 10.1021/ac0702084.

[57] D. F. Swinehart, 'The Beer-Lambert Law', *J. Chem. Educ.*, vol. 39, no. 7, p. 333, Jul. 1962, doi: 10.1021/ed039p333.

[58] R. Javed, M. Zia, S. Naz, S. O. Aisida, N. ul Ain, and Q. Ao, 'Role of capping agents in the application of nanoparticles in biomedicine and environmental remediation: recent trends and future prospects', *Journal of Nanobiotechnology*, vol. 18, no. 1, p. 172, Nov. 2020, doi: 10.1186/s12951-020-00704-4.

[59] D. P. Stankus, S. E. Lohse, J. E. Hutchison, and J. A. Nason, 'Interactions between Natural Organic Matter and Gold Nanoparticles Stabilized with Different Organic Capping Agents', *Environ. Sci. Technol.*, vol. 45, no. 8, pp. 3238–3244, Apr. 2011, doi: 10.1021/es102603p.

[60] Y. Wang *et al.*, 'Aggregation affects optical properties and photothermal heating of gold nanospheres', *Sci Rep*, vol. 11, no. 1, p. 898, Jan. 2021, doi: 10.1038/s41598-020-79393-w.

[61] A. Tukova, N. T. T. Nguyen, A. Garcia-Bennett, A. Rodger, and Y. Wang, 'Plasmonic Nanostars: Unique Properties That Distinguish Them from Spherical Nanoparticles from a Biosensing Perspective', *Advanced Optical Materials*, vol. n/a, no. n/a, p. 2401183, doi: 10.1002/adom.202401183.

[62] F. Hao, C. L. Nehl, J. H. Hafner, and P. Nordlander, 'Plasmon Resonances of a Gold Nanostar', *Nano Lett.*, vol. 7, no. 3, pp. 729–732, Mar. 2007, doi: 10.1021/nl062969c.

[63] 'Surface Modification of Gold Nanoprisms and Their Self-Assembly with Nanospheres - Zámbó - 2023 - Particle & Particle Systems Characterization - Wiley Online Library'. Accessed: Sep. 07, 2024. [Online]. Available: https://onlinelibrary.wiley.com/doi/full/10.1002/ppsc.202200197

[64] C. G. Sanz, D. N. Crisan, R. J. B. Leote, M. Onea, and M. M. Barsan, 'Bioconjugates of mercaptocarboxylic acids functionalized AuNP and superoxide dismutase for superoxide electrochemical monitoring', *Microchim Acta*, vol. 189, no. 7, p. 245, Jun. 2022, doi: 10.1007/s00604-022-05352-z.

[65] 'FAQ: Peak size or z-average size - which one to pick in DLS? | Malvern Panalytical'. Accessed: Sep. 21, 2024. [Online]. Available: https://www.malvernpanalytical.com/en/learn/knowledge-center/insights/faq-peak-size-or-z-average-size-which-one-to-pick-in-dls

[66] S. Dominguez-Medina, J. Blankenburg, J. Olson, C. F. Landes, and S. Link, 'Adsorption of a Protein Monolayer via Hydrophobic Interactions Prevents Nanoparticle Aggregation under Harsh Environmental Conditions', *ACS Sustainable Chem. Eng.*, vol. 1, no. 7, pp. 833–842, Jul. 2013, doi: 10.1021/sc400042h.

[67] S. Okyem, O. Awotunde, T. Ogunlusi, M. B. Riley, and J. D. Driskell, 'Probing the Mechanism of Antibody-Triggered Aggregation of Gold Nanoparticles', *Langmuir*, vol. 37, no. 9, pp. 2993–3000, Mar. 2021, doi: 10.1021/acs.langmuir.1c00100.

[68] L. Zhang, Y. Mazouzi, M. Salmain, B. Liedberg, and S. Boujday, 'Antibody-Gold Nanoparticle Bioconjugates for Biosensors: Synthesis, Characterization and Selected Applications', *Biosensors and Bioelectronics*, vol. 165, p. 112370, Oct. 2020, doi: 10.1016/j.bios.2020.112370.

[69] R. Maier, M. R. Fries, C. Buchholz, F. Zhang, and F. Schreiber, 'Human versus Bovine Serum Albumin: A Subtle Difference in Hydrophobicity Leads to Large Differences in Bulk and Interface Behavior', *Crystal Growth & Design*, vol. 21, no. 9, pp. 5451–5459, Sep. 2021, doi: 10.1021/acs.cgd.1c00730.

[70] H.-Q. Wang and Z.-X. Deng, 'Gel electrophoresis as a nanoseparation tool serving DNA nanotechnology', *Chinese Chemical Letters*, vol. 26, no. 12, pp. 1435–1438, Dec. 2015, doi: 10.1016/j.cclet.2015.10.019.

[71] P. Serwer and G. A. Griess, 'Advances in the separation of bacteriophages and related particles', *Journal of Chromatography B: Biomedical Sciences and Applications*, vol. 722, no. 1–2, pp. 179–190, Feb. 1999, doi: 10.1016/S0378-4347(98)00404-6.

[72] C. Hasenoehrl, C. M. Alexander, N. N. Azzarelli, and J. C. Dabrowiak, 'Enhanced detection of gold nanoparticles in agarose gel electrophoresis', *Electrophoresis*, vol. 33, no. 8, pp. 1251–1254, Apr. 2012, doi: 10.1002/elps.201100556.

[73] J. X. Xu, M. S. Alom, R. Yadav, and N. C. Fitzkee, 'Predicting protein function and orientation on a gold nanoparticle surface using a residue-based affinity scale', *Nat Commun*, vol. 13, no. 1, p. 7313, Nov. 2022, doi: 10.1038/s41467-022-34749-w.

[74] G. Ruiz, N. Ryan, K. Rutschke, O. Awotunde, and J. D. Driskell, 'Antibodies Irreversibly Adsorb to Gold Nanoparticles and Resist Displacement by Common Blood Proteins', *Langmuir*, vol. 35, no. 32, pp. 10601–10609, Aug. 2019, doi: 10.1021/acs.langmuir.9b01900.

[75] A. Dalot, 'PLASMONIC NANOSTARS FOR SENSITIVE SERSBASED IMMUNODETECTION'.

[76] M. J. Oliveira, 'NANOSERS MICROFLUIDICS PLATFORM FOR RAPID SCREENING FOR INFECTIOUS DISEASES'.

[77] K. Tripathi and J. D. Driskell, 'Quantifying Bound and Active Antibodies Conjugated to Gold Nanoparticles: A Comprehensive and Robust Approach To Evaluate Immobilization Chemistry', *ACS Omega*, vol. 3, no. 7, pp. 8253–8259, Jul. 2018, doi: 10.1021/acsomega.8b00591.

[78] M. J. Pollitt, G. Buckton, R. Piper, and S. Brocchini, 'Measuring antibody coatings on gold nanoparticles by optical spectroscopy', *RSC Adv.*, vol. 5, no. 31, pp. 24521–24527, Mar. 2015, doi: 10.1039/C4RA15661G.

[79] 'Dynamic light scattering common terms defined'.

[80] M. J. Oliveira *et al.*, 'Design and Simple Assembly of Gold Nanostar Bioconjugates for Surface-Enhanced Raman Spectroscopy Immunoassays', *Nanomaterials (Basel)*, vol. 9, no. 11, p. 1561, Nov. 2019, doi: 10.3390/nano9111561.

[81] M. Rabe, D. Verdes, and S. Seeger, 'Understanding protein adsorption phenomena at solid surfaces', *Advances in Colloid and Interface Science*, vol. 162, no. 1–2, pp. 87–106, Feb. 2011, doi: 10.1016/j.cis.2010.12.007.

[82] D. Vincent, A. Elkins, M. R. Condina, V. Ezernieks, and S. Rochfort, 'Quantitation and Identification of Intact Major Milk Proteins for High-Throughput LC-ESI-Q-TOF MS Analyses', *PLoS One*, vol. 11, no. 10, p. e0163471, Oct. 2016, doi: 10.1371/journal.pone.0163471.

[83] A. L. Tomás *et al.*, 'Development of a Gold Nanoparticle-Based Lateral-Flow Immunoassay for Pneumocystis Pneumonia Serological Diagnosis at Point-of-Care', *Front. Microbiol.*, vol. 10, Dec. 2019, doi: 10.3389/fmicb.2019.02917.

[84] S. Binder and J. A. Isler, 'Detection of Antibodies Relevant to Infectious Disease', in *The Immunoassay Handbook*, Elsevier, 2013, pp. 149–155. doi: 10.1016/B978-0-08-097037-0.00011-7.

[85] M. Gellner, K. Kömpe, and S. Schlücker, 'Multiplexing with SERS labels using mixed SAMs of Raman reporter molecules', *Anal Bioanal Chem*, vol. 394, no. 7, pp. 1839–1844, Aug. 2009, doi: 10.1007/s00216-009-2868-8.

[86] 'Nitrocellulose Membrane'. Accessed: Sep. 23, 2024. [Online]. Available: https://mdimembrane.com/products/product-by-industry/rapid-diagnostics/rapid-immunoassays/lateral-flow-tests/nitrocellulose-membrane

[87] S. Srivastav *et al.*, 'Rapid and Sensitive SERS-Based Lateral Flow Test for SARS-CoV2-Specific IgM/IgG Antibodies', *Anal. Chem.*, vol. 93, no. 36, pp. 12391–12399, Sep. 2021, doi: 10.1021/acs.analchem.1c02305.